Supersonic Modes in Hot-Wall Hypersonic Boundary Layers with Thermochemical Nonequilibrium Effects

Carleton P. Knisely* and Xiaolin Zhong†

University of California, Los Angeles, California, 90095, USA

There has been a renewed interest in studying the stability of the supersonic mode in hypersonic boundary layers. The supersonic mode, sometimes also referred to as the spontaneous radiation of sound, is associated with an unstable Mack's second mode synchronizing with the slow acoustic spectrum, causing the disturbance to travel upstream supersonically relative to the meanflow outside the boundary layer. Recent theoretical results have shown the possibility of the supersonic mode existing in hot-wall flows, which is contrary to the known research on the supersonic mode suggesting it is an artifact of hypersonic cold-wall ($T_w/T_\infty < 1$) flows. This work aims to use thermochemical nonequilibrium Direct Numerical Simulation (DNS) along with thermochemical nonequilibrium Linear Stability Theory (LST) to replicate the flow conditions used in the theoretical study to obtain a more complete investigation of the supersonic mode in hot-wall flow conditions. The simulation is Mach 10 flow over a 1mm nose radius axisymmetric cone. LST results indicate that the supersonic mode does not exist in the hot-wall flow, however unsteady DNS results indicate the presence of the spontaneous radiation of sound, going against LST predictions. Further FFT analysis indicated that this sound radiation was an artifact of the interaction of stable mode S and mode F1 with the slow acoustic spectrum. This interaction very briefly produced the unstable supersonic mode. The supersonic mode quickly became stable after its initial creation, and the sound radiation ceased. As mentioned in previous research, the sound radiation may act as an energy sink and can cause an asymmetric frequency response to the disturbance. The complex interaction of modes implies the traditional transition prediction tools like LST used in the e^N method may not be suitable for use in these types of flows.

I. Introduction

It has long been known that boundary layer transition from laminar to turbulent has a considerable impact on the design of hypersonic vehicles. Transition to turbulent flow drastically increases drag and heating to the vehicle surface, and can have a prominent effect on control of the hypersonic vehicle. It also affects engine performance and operability as well as vehicle structure and weight. The heating to the vehicle surface is one of the primary considerations in hypersonic vehicle design. Thermal protection systems (TPSs) are required to prevent the surface of the vehicle from overheating and failing. TPSs are usually specified with a large factor of safety to ensure protection of the vehicle, although this often adds unnecessary weight, reducing the maximum payload. The ability to predict accurately or even to delay the onset of transition and maintain laminar flow can have a significant payoff in terms of the reduction in aerodynamic heating, higher fuel efficiency, and weight of the thermal protection system.

Mack[1] found that the major instability waves leading to transition to turbulence in a perfect gas flow are the first and second modes, which Fedorov[2] recently described as acoustic rays physically trapped between the wall and sonic line. Researchers have subsequently developed numerical tools to predict transition to turbulence due to the first and second mode. Malik[3] implemented multiple numerical methods for solving the Linear Stability Theory (LST) equations for a perfect gas. Chemical nonequilibrium effects in the LST framework were studied numerically by Stuckert and Reed.[4] Hudson et al.[5] incorporated thermal nonequilibrium effects in addition to chemical nonequilibrium for LST. Johnson et al.[6–8] studied hypersonic boundary

*Graduate Student, Mechanical and Aerospace Engineering, carleton.knisely@gmail.com, AIAA Student Member.

†Professor, Mechanical and Aerospace Engineering, xiaolin@seas.ucla.edu, AIAA Associate Fellow.

layer transition in thermochemical nonequilibrium using the Parabolized Stability Equations (PSE), which account for nonparallel flow effects that are ignored in LST. Overall, the researchers determined that dissociation of air species is stabilizing to the first mode, but destabilizing to the second mode. Additionally, it was determined that thermal nonequilibrium has a slight destabilizing effect on the first mode, and a slight stabilizing effect on the second mode. These contemporary studies have primarily focused on flows with relatively modest levels of wall cooling with the wall-to-edge temperature ratio greater than unity. ($T_w/T_e > 1$). This motivated Bitter and Shepherd[9] to examine the effect of highly cooled walls on hypersonic boundary layer stability.

Flows with highly cooled walls are of interest in high-enthalpy flows, such as shock tube experiments in which the wall temperature remains ambient during the short test duration, as well as some real flight cases.[10,11] It has long been known through studies by Lees[12] and Mack[13,14] that wall cooling stabilizes the first mode but destabilizes the second mode. Bitter and Shepherd[9] took these studies a few steps further and have shown through a chemical equilibrium, thermal nonequilibrium LST analysis that high levels of wall cooling on a flat plate lead to unique features, in particular an unstable second mode traveling upstream supersonically relative to the free stream. The supersonic modes cause second-mode instabilities over a wider range of frequencies than subsonic modes. The unstable supersonic modes cause acoustic waves to radiate from the wall into the free stream. This phenomenon has been referred to as the spontaneous radiation of sound.[15] Figure 1 compares contours of temperature fluctuations at two different locations and frequencies. Note that the perturbations are confined to within the boundary layer for the subsonic mode, but extend well into the free stream for the supersonic mode.

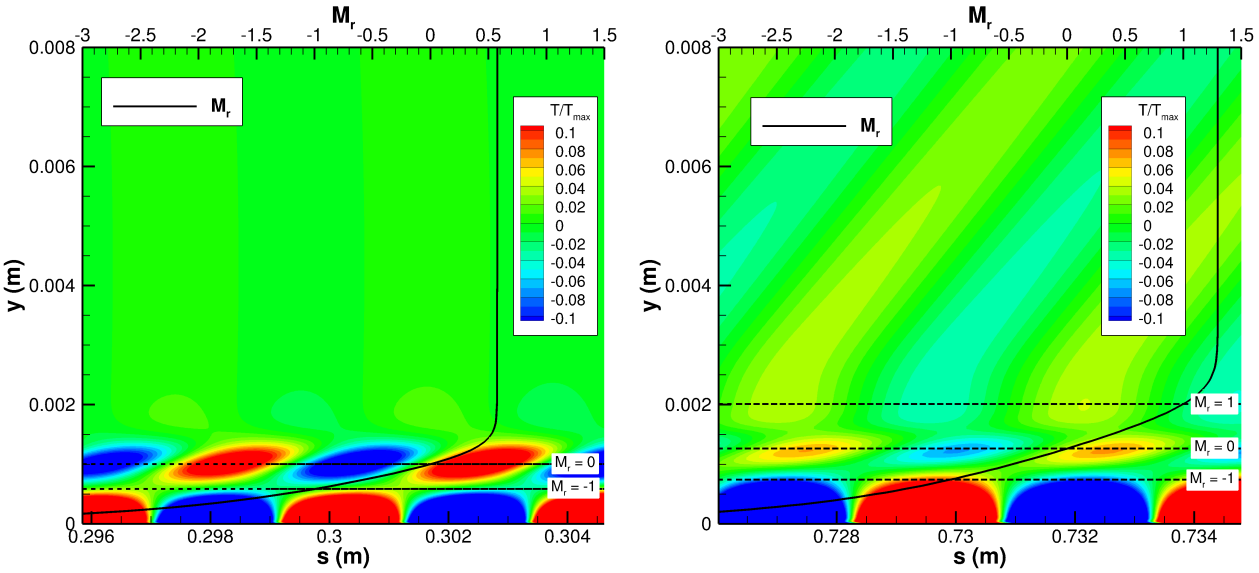

(a) (b)

Figure 1: Contours of temperature fluctuations. $T_w/T_\infty = 0.2$, $T_w = 300K$, $M_\infty = 5$: (a) Subsonic mode: $s = 0.302$m, $f = 800$ kHz. (b) Supersonic mode: $s = 0.733$m, $f = 550$ kHz.[16]

A schematic of the supersonic mode is presented in Figure 2 for further elaboration. A useful parameter describing the speed of propagation of the disturbance relative to the mean flow is the relative Mach number

$$M_r(y) = \frac{\overline{u}(y) - c_r}{\overline{a}(y)} \tag{1}$$

where $\overline{u}(y)$ is the local mean flow velocity tangential to the wall, $c_r = \omega/\sqrt{\beta^2 + \alpha_r^2}$ is the disturbance propagation speed, and $\overline{a}(y)$ is the local mean flow speed of sound. Near the wall, $\overline{u}$ is small and the disturbance is traveling supersonically downstream relative to the mean flow, indicated below a relative Mach number of $M_r < -1$. The sonic line $M_r = -1$ acts as a wave guide for the acoustic rays,[2] resulting in the traditional Mack modes. Outside of $M_r = -1$, the disturbance is traveling subsonically with respect to the

freestream, and creates a "rope-like" wave pattern observed by many researchers both experimentally[17,18] and numerically.[19–21] In some flows (specific flow conditions to be examined), a second supersonic region can be present. Previous researchers[9] have attributed this second supersonic region to a highly-cooled wall, however this may not always be the case. Outside of $M_r = 1$, the disturbance is traveling upstream supersonically with respect to the freestream. This creates the "slanted" wave pattern outside of the boundary layer shown in Figure 1(b). The angle created by this wave pattern is analogous to a Mach wave angle from traditional compressible flow theory, and is given by $\mu = \arcsin(1/M_r)$.

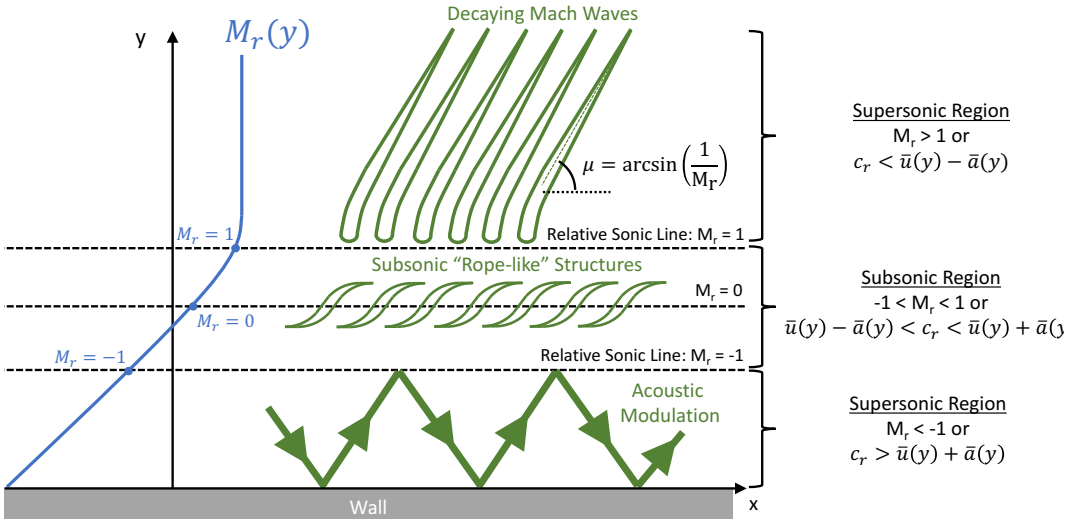

Figure 2: Schematic of supersonic mode.

Chuvakhov and Fedorov[15] confirmed Bitter and Shepherd's[9] findings through LST analysis as well as unsteady direct numerical simulation (DNS) analysis. Knisely and Zhong[16] have subsequently extended the study of the supersonic mode to a blunt cone using thermochemical nonequilibrium DNS and LST analyses, and determined the relative Mach number to be a critical parameter in the behavior of the boundary layer disturbance. Supersonic modes are not a new finding, however, and have in fact been identified in a number of other flow configurations. Mack[13] commented on neutral supersonic waves in flow over a flat plate. Chang, Vinh, and Malik[22] reported supersonic modes in Mach 20 flow over a 6 degree wedge with wall temperature ratio $T_w/T_{ad} = 0.1$. Fedorov, Soudakov, and Leyva[23] found unstable supersonic modes in flow with gas injection. Fedorov et al.[24] encountered unstable supersonic modes in flow with resonating microcavities. Bres et al.[25] also found this phenomenon in flow over a wall with a porous coating. Wagnild[26] observed the spontaneous radiation of sound, although the focus of his study was the effect of vibrational nonequilibrium. Salemi et al. modeled configurations typical of the T5 tunnel at Caltech and investigates second mode synchronization with the slow acoustic spectrum. They investigated the effect of nonlinear disturbances,[27,28] a flared cone geometry,[29] and high-temperature effects,[30] although the Prandtl number and ratio of specific heats were fixed in their real gas model.

Despite the evidence presented by Bitter and Shepherd[9] and Chuvakhov and Fedorov,[15] it is possible that the impact of the highly-cooled wall on the spontaneous radiation of sound may have been overstated because chemical nonequilibrium was not accounted for. Recent theoretical results by Anatoli Tumin[31,32] indicate the spontaneous radiation of sound in flows with $T_w/T_e > 1$. Edwards and Tumin[32] recently conducted a numerical study of boundary layer receptivity to kinetic fluctuations, in which all external forcing (freestream waves and surface disturbances) is negligible. Instead, additional fluctuating terms appear in the momentum and energy equations using the same formulation as Fedorov and Tumin.[33] Edwards and Tumin[32] found that the supersonic mode existed in hot-wall flows only when chemical nonequilibrium effects were included in the meanflow calculation, but nonequilibrium effects in the stability solver were not as significant. Specifically, the supersonic mode was prominent on a $T_w = 1000$ K isothermal flat plate with boundary layer edge conditions $T_e = 834$ K, $p_e = 0.0433$ atm, and $M_e = 9.91$. Edwards and Tumin[32] suggested that the chemical nonequilibrium effects in the meanflow may have a significant role in the creation of the supersonic mode in hot-wall flows. This study aims to examine the impact of real gas effects on the mechanism of the creation of

the spontaneous radiation of sound through DNS and LST studies of a blunt cone with similar flow conditions as Edwards and Tumin.[32]

II. Simulation Conditions

The flow conditions for this study are summarized in Table 1 and are intended to be similar to "Case 3" of Edwards and Tumin.[32] The geometry is a 5 degree half-angle axisymmetric blunt cone 1 meter in length with a nose radius of 1 mm. The DNS simulation used 256 points in the wall-normal direction and roughly 5 points per millimeter on the surface of the cone in the streamwise direction. In the azimuthal direction, four points are used. LST simulations interpolated the DNS meanflow onto the LST grid defined by the stretching methods discussed in the following sections.

Table 1: Flow conditions for DNS simulation.

Parameter	Value
M_∞	10
$H_{0,\infty}$	14.78 MJ/kg
ρ_∞	1.91 E-2 kg/m^3
p_∞	4 kPa
T_w	1000 K
T_w/T_∞	1.43

As will be explained in the following sections, the DNS code used in this study utilizes a shock-fitting method. Thus, the parameters in Table 1 are the free stream conditions upstream of the shock formed over the body.

III. Governing Equations and Gas Model

The governing equations for the DNS and LST codes are those developed by Mortensen and Zhong,[34–39] which are formulated for thermochemical nonequilibrium assuming a two-temperature model. Their formulation is presented here for clarity. The rotational mode is assumed to be fully excited with up to eleven non-ionizing species with finite-rate chemistry. Two-temperatures are used to represent translation-rotation energy and vibration energy. There are two species models: an eleven-species model (N_2, O_2, NO, C_3, CO_2, C_2, CO, CN, N, O, C) used for ablation studies and a five-species model (N_2, O_2, NO, N, and O) used to simulate air. The five species model is used here. The Navier-Stokes equations in conservative form consist of five species mass conservation equations, three momentum conservation equations, the total energy equation, and the vibration energy equation. The governing equations in vector form are written as

$$\frac{\partial U}{\partial t} + \frac{\partial F_j}{\partial x_j} + \frac{\partial G_j}{\partial x_j} = W \tag{2}$$

where U is the state vector of conserved quantities and W is the source terms defined by

$$U = \begin{bmatrix} \rho_1 \\ \vdots \\ \rho_{ns} \\ \rho u_1 \\ \rho u_2 \\ \rho u_3 \\ \rho e \\ \rho e_v \end{bmatrix}, \quad W = \begin{bmatrix} \omega_1 \\ \vdots \\ \omega_{ns} \\ 0 \\ 0 \\ 0 \\ 0 \\ \sum_{s=1}^{nms} \left(Q_{T-V,s} + \omega_s e_{v,s} \right) \end{bmatrix}.$$

The inviscid and viscous flux vectors, F_j and G_j, respectively, are defined by

$$F_j = \begin{bmatrix} \rho_1 u_j \\ \vdots \\ \rho_{ns} u_j \\ \rho u_1 u_j + p\delta_{1j} \\ \rho u_2 u_j + p\delta_{2j} \\ \rho u_3 u_j + p\delta_{3j} \\ (p + \rho e)\, u_j \\ \rho e_v u_j \end{bmatrix}, \quad G_j = \begin{bmatrix} \rho_1 v_{1j} \\ \vdots \\ \rho_{ns} v_{nsj} \\ \tau_{1j} \\ \tau_{2j} \\ \tau_{3j} \\ -u_i\tau_{ij} - k_T \frac{\partial T}{\partial x_j} - k_V \frac{\partial T_V}{\partial x_j} + \sum_{s=1}^{nms} \rho_s h_s v_{sj} \\ -k_V \frac{\partial T_V}{\partial x_j} + \sum_{s=1}^{nms} \rho_s e_{v,s} v_{sj} \end{bmatrix}.$$

where v_{sj} is the species diffusion velocity, and

$$\tau_{ij} = \mu \left(\frac{\partial u_i}{\partial x_j} + \frac{\partial u_j}{\partial x_i} \right) - \frac{2}{3} \mu \frac{\partial u_k}{\partial x_k} \delta_{ij} \tag{3}$$

is the viscous stress. The total energy per unit volume, ρe, is defined as

$$\rho e = \sum_{s=1}^{ns} \rho_s c_{v,s} T + \rho e_v + \frac{1}{2} \rho \left(u_1^2 + u_2^2 + u_3^2 \right) + \sum_{s=1}^{ns} \rho_s h_s^o \tag{4}$$

where h_s^o is the species heat of formation, $e_{v,s}$ is the species specific vibration energy, and $c_{v,s}$ is the species translation-rotation specific heat at constant volume, defined as

$$c_{v,s} = \begin{cases} \frac{5}{2} \frac{\mathcal{R}}{M_s} & s = 1, 2, \ldots, nms \\ \frac{3}{2} \frac{\mathcal{R}}{M_s} & s = nms + 1, \ldots, ns. \end{cases} \tag{5}$$

The vibration energy per unit volume, ρe_v, is defined as

$$\rho e_v = \sum_{s=1}^{nms} \rho_s e_{v,s} = \sum_{s=1}^{nms} \rho_s \frac{\mathcal{R}}{M_s} \frac{\theta_{v,s}}{\exp\left(\theta_{v,s}/T_V\right) - 1} \tag{6}$$

where $\theta_{v,s}$ denotes the characteristic vibrational temperature of each vibrational mode. The characteristic vibration temperatures are taken from Park.[40]

To model chemical nonequilibrium, three dissociation reactions and three exchange reactions are used. Each reaction is governed by a forward and backward reaction rate determined from

$$k_f = C_f T_a^{\eta} \exp\left(-\theta_d / T_a\right) \tag{7}$$

$$k_b = k_f / K_{eq} \tag{8}$$

where all forward reaction rates are obtained from Park.[40] The equilibrium coefficient, K_{eq}, is determined using

$$K_{eq} = A_0 \exp\left(\frac{A_1}{Z} + A_2 + A_3 \ln(Z) + A_4 Z + A_5 Z^2 \right), \quad Z = \frac{10000}{T} \tag{9}$$

which is a curve fit to experimental data from Park.[40]

The Landau-Teller formulation is used to calculate the source term in the vibration energy equation representing the exchange of energy between the translation-rotation and vibration energies

$$Q_{T-V,s} = \rho_s \frac{e_{v,s}(T) - e_{v,s}(T_V)}{< \tau_s > + \tau_{cs}} \tag{10}$$

where $< \tau_s >$ is the Landau-Teller relaxation time given by Lee.[41] The term τ_{cs} is from Park[40] to more accurately model the relaxation time in areas of high temperatures occurring just downstream of the bow shock.

The viscosity of each species is computed using a Blottner curve fit shown in Eq. 11. The coefficients are obtained from Blottner et al.[42] The mixture viscosity is then found using each species viscosity from Wilke's[43] mixing rule (Eq. 12). The total heat conductivities for each energy mode are computed in a similar fashion as viscosity. The diffusion velocity is calculated using Fick's law and a constant Schmidt number of 0.5.

$$\mu_s = 0.1 \exp\left[(A_s^\mu \ln(T) + B_s^\mu)\ln(T) + C_s^\mu\right] \tag{11}$$

$$\mu = \sum_{s=1}^{ns} \frac{X_s \mu_s}{\phi_s} \tag{12}$$

$$X_s = \frac{c_s}{M_s} \tag{13}$$

$$\phi_s = \frac{\sum_{r=1}^{ns} X_r \left[1 + \left(\frac{M_s}{M_r}\right)^{1/4}\right]^2}{\left[8\left(1 + \frac{M_s}{M_r}\right)\right]^{1/2}} \tag{14}$$

IV. Numerical Methods

A. DNS

The thermochemical nonequilibrium code developed by Mortensen and Zhong[34–39] utilizes a high-order shock-fitting method extended from a perfect gas flow version by Zhong[44] to compute the flow field between the shock and the body. The numerical method is repeated here for clarity. For shock-fitting computations the shock location is not known *a priori*, so its position is solved along with the flow field. Since the shock position is not stationary, the grid used to compute the flow field is a function of time. This leads to the coordinate transformation

$$\begin{cases} \xi = \xi(x,y,z) \\ \eta = \eta(x,y,z,t) \\ \zeta = \zeta(x,y,z) \\ \tau = t \end{cases} \iff \begin{cases} x = x(\xi,\eta,\zeta,\tau) \\ y = y(\xi,\eta,\zeta,\tau) \\ z = z(\xi,\eta,\zeta,\tau) \\ t = \tau \end{cases} \tag{15}$$

where y is normal to the body, x is in the streamwise direction, z is in the transverse direction, $\zeta_t = 0$, and $\xi_t = 0$. The governing equation can then be transformed into computational space as

$$\frac{1}{J}\frac{\partial U}{\partial \tau} + \frac{\partial E'}{\partial \xi} + \frac{\partial F'}{\partial \eta} + + \frac{\partial G'}{\partial \zeta} + \frac{\partial E'_v}{\partial \xi} + \frac{\partial F'_v}{\partial \eta} + + \frac{\partial G'_v}{\partial \zeta} + U\frac{\partial (1/J)}{\partial \tau} = \frac{W}{J} \tag{16}$$

where J is the Jacobian of the coordinate transformation and

$$E' = \frac{F_1\xi_x + F_2\xi_y + F_3\xi_z}{J} \tag{17}$$

$$F' = \frac{F_1\eta_x + F_2\eta_y + F_3\eta_z}{J} \tag{18}$$

$$G' = \frac{F_1\zeta_x + F_2\zeta_y + F_3\zeta_z}{J} \tag{19}$$

$$E'_v = \frac{G_1\xi_x + G_2\xi_y + G_3\xi_z}{J} \tag{20}$$

$$F'_v = \frac{G_1\eta_x + G_2\eta_y + G_3\eta_z}{J} \tag{21}$$

$$G'_v = \frac{G_1\zeta_x + G_2\zeta_y + G_3\zeta_z}{J}. \tag{22}$$

A seven point stencil is used to discretize the spatial derivatives

$$\frac{\partial f_i}{\partial x} = \frac{1}{hb_i}\sum_{k=-3}^{3}\alpha_{i+k}f_{i+k} - \frac{\alpha}{6!b_i}h^5\left(\frac{\partial f^6}{\partial^6 x}\right) \tag{23}$$

where

$$\begin{aligned} \alpha_{i\pm3} &= \pm1 + \frac{1}{12}\alpha, & \alpha_{i\pm2} &= \mp9 - \frac{1}{2}\alpha \\ \alpha_{i\pm1} &= \pm45 + \frac{5}{4}\alpha, & \alpha_i &= -\frac{5}{3}\alpha \\ b_i &= 60 \end{aligned}$$

and where h is the step size, $\alpha < 0$ is a fifth order upwind explicit scheme, and $\alpha = 0$ reduces to a sixth order central scheme. Here the inviscid terms use $\alpha = -6$ which yields a low dissipation fifth order upwinded difference and the viscous terms are discretized using $\alpha = 0$. The derivatives in the transverse direction, if required, are treated with Fourier collocation. To compute second derivatives, the first order derivative operator is applied twice.

Flux splitting is used for the inviscid flux terms resulting in

$$F' = F'^{+} + F'^{-} \tag{24}$$

where

$$F'^{\pm} = \frac{1}{2}(F' \pm \Lambda U) \tag{25}$$

and Λ is a diagonal matrix that ensures F'^{+} and F'^{-} contain only pure positive and negative eigenvalues, respectively. For thermochemical nonequilibrium, the eigenvalues of Λ were derived by Liu and Vinokur.[45]

Conditions behind the shock are calculated from Rankine-Hugoniot relations. In the freestream, the flow is assumed to be in thermal equilibrium and the chemical composition of the flow is frozen. The shock is assumed to be infinitely thin which means that the flow has no time to relax as it crosses the shock as relaxation rates are finite. This leads to the chemical composition remaining constant across the shock, as well as the vibration temperature. Since neither process has any time to relax across the shock, the relaxation zone is entirely downstream of the shock. A complete derivation of thermochemical nonequilibrium shock fitting can be found in Prakash et al.[46] A low storage 3rd-order Runge-Kutta method from Williamson[47] is used to advance the solution in time.

B. LST

The linear stability analysis used here is largely based on the LST code developed by Mortensen,[39] however here the assumption of zero wall-normal velocity is relaxed (i.e. $\overline{v} \neq 0$), and new freestream boundary conditions incorporating a shock at the computational boundary are used. A body-fitted orthogonal curvilinear coordinate system is used for axisymmetric bodies where x is in the streamwise direction, y is in the wall-normal direction, z is in the transverse direction, and the origin is located on the body surface. Curvature in the streamwise and transverse directions is included similar to Malik and Spall.[48] Elemental lengths are defined as $h_1 dx$, dy, and $h_3 dz$ where

$$h_1 = 1 + \kappa y \tag{26}$$

$$h_3 = r_b + y\cos(\theta) \tag{27}$$

and where κ is the streamwise curvature, r_b is the local radius of the body, and θ is the local half angle of the body. The coordinate system for a flat plate is recovered by setting h_1 and h_3 to unity. For a straight cone, only h_3 is required and h_1 is set to unity.

The derivation of the thermochemical nonequilibrium LST equations follows the work of Hudson.[5,49] The main difference in the derivation is that here the equation for each species velocity is substituted into the governing equations before they are linearized, similar to Klentzman et al.[50] The LST equations are derived from the governing equations (Eq. 2) where the instantaneous flow is comprised of a mean and fluctuating component $q = \overline{q} + q'$. Here q represents any flow variable such as velocity, density, temperature, etc. The instantaneous flow is then substituted into the governing equations where the steady flow is assumed to

satisfy the governing equations and is subtracted out. The mean flow is assumed to be a function of y only i.e. $\overline{q}(x,y,z) = \overline{q}(y)$ and the flow disturbances are assumed to be small i.e. linear. The perturbations are then assumed to be in the form of a normal mode described by

$$q' = \hat{q}(y) \exp\left[i\left(\alpha x + \beta z - \omega t\right)\right] \tag{28}$$

where ω is the circular frequency of the disturbance and α and β are the wavenumbers. Commonly ω and β are assumed to be real and the wavenumber α is assumed to be complex which means the disturbances grow in space rather than time. If ω is complex and α and β are real then the disturbances grow in time rather than space. For comparison to direct numerical simulation the spatial stability approach is used i.e. α is complex which results in the dispersion relation $\alpha = \Omega(\omega, \beta)$. Substituting in the normal mode form for the perturbation reduces the problem to a coupled set of $ns + 5$ ordinary differential equations

$$\left(\mathbf{A}\frac{d^2}{dy^2} + \mathbf{B}\frac{d}{dy} + \mathbf{C}\right)\vec{\phi} = \vec{0}. \tag{29}$$

where $\vec{\phi} = \left[\hat{\rho}_1, \hat{\rho}_2, \ldots, \hat{\rho}_{ns}, \hat{u}, \hat{v}, \hat{w}, \hat{T}, \hat{T}_V\right]^T$ and $\mathbf{A}$, $\mathbf{B}$ and $\mathbf{C}$ are complex square matrices of size $ns+5$. This is now a boundary value problem where the derivative operators can be discretized and the equations solved numerically.

For hypersonic compressible boundary layers it is important to have high grid resolution near the generalized inflection point.[1] The grid used by Mortensen[39] uses two different functions to cluster points around the inflection point and near the wall. It is called the cosine-exponential grid. For some boundary layers, there is a sharp increase in the eigenfunctions near the wall for the temperatures and densities that was not captured correctly with the grid that only clustered points near the inflection point, such as a grid similar to the one used by Hudson et al.[5] Mortensen's[39] cosine-exponential grid was much more effective for boundary layers with strong changes in the eigenfunctions near the wall.

In hypersonic flows in which the spontaneous radiation of sound occurs, the cosine-exponential grid may not provide enough grid resolution in the free stream or near the outer shock boundary. The continuous modes oscillate to the computational boundary in many cases. Therefore, it is helpful to use an additional exponential grid stretching function at the edge of the computational boundary. This second exponential grid stretching function gave better grid spacing in the freestream and clustered points near the edge of the computational boundary, which is desirable when a shock coincides with the boundary. The cosine-double-exponential grid retains the benefits of capturing the sharp increases in eigenfunctions at the wall and at the generalized inflection point, while adding additional resolution in the freestream and near the outer edge boundary.

With the grid defined, Eq. 29 can be transformed into computational space and a numerical representation of the derivatives can be given. The first and second derivative operators in the wall-normal direction are discretized by taking derivatives of Lagrange polynomials in physical space. These derivative operators are applied in physical space rather than computational space to avoid Runges phenomena where spurious oscillations can occur for a one-sided stencil with a high order of approximation. Mortensen's[39] scheme can be applied for variable stencil sizes and can be used to obtain high-order approximations. Here, a five-point stencil is used, resulting in a 4th order method similar to the one used by Malik.[3]

After discretization, nonlinearities exist in α so the global method suggested by Malik[3] is used to compute the eigenvalue spectrum with $\alpha^2 = 0$. This method computes the eigenvalues from a generalized eigenvalue problem $\tilde{A}\vec{\phi} = \alpha\tilde{B}\vec{\phi}$ where the LAPACK[51] subroutine ZGGEV is used here for solution. From the eigenvalue spectrum an initial guess can be obtained for the local method which results in $\overline{A}\vec{\phi} = \overline{B}$ and the eigenvalue is found iteratively without dropping the α^2 terms. The LAPACK subroutine ZGESV is used to solve the local problem. It is also possible to avoid the computationally intensive global method and obtain an initial guess for α from a nearby streamwise location or a DNS simulation assuming the unsteady DNS results are available.

The boundary conditions are required for the freestream and the wall. The wall boundary conditions are linearized non-catalytic conditions for density, no slip, and zero temperature perturbation, although more complex surface boundary conditions can be used for ablation studies.[35,39] In the freestream, the shock boundary conditions developed by Knisely and Zhong[16] were considered, however they had virtually no impact on the stability results because the supersonic mode was shown not to exist in the LST results. Therefore, the standard "zero" boundary conditions in the freestream were suitable for this study.

LST gives information about what disturbance frequencies are unstable and the corresponding growth rates of those frequencies, but there is no information on the amplitude of the incoming disturbance. To estimate boundary-layer transition using LST, the e^N transition criterion is used which is defined as

$$e^N = \frac{A(s)}{A_0} = \exp\left[\int_{s_0}^{s} -\alpha_i(s,f)ds\right] \tag{30}$$

where $A(s)$ is the integrated disturbance amplitude, A_0 is the initial disturbance amplitude, s_0 is the location where the disturbance first becomes unstable, and α_i is the spatial amplification rate obtained from LST. The integration is performed for a constant frequency f, and is done numerically using trapezoidal integration. Note that a negative imaginary part of the wave number α results in disturbance growth while a positive value results in disturbance decay. The N-factor is specifically the exponent of e^N. In-flight transition N-factors are commonly understood to be around 10. Malik[11] showed that 9.5 and 11.2 correlated with transition onset for two high Mach number flight tests. In ground test facilities the transition N-factor is usually lower.

V. Steady DNS Results

The Mach 10 flow over a hot-wall ($T_w/T_\infty = 1.43$) cone produced significant thermochemical nonequilibrium in the nose region. Steady DNS translation-rotation temperature, vibration temperature, and mass fraction contours for the nose region of the cone are shown in Figure 3. Figures 3a and 3b indicate the flow is in thermal nonequilibrium in the nose region, and Figures 3c and 3d indicate the flow is in chemical nonequilibrium. Specifically, O_2 dissociation is the predominant reaction in this flow field, with O_2 mass fraction going nearly to zero near the stagnation point. N_2 dissociation is not negligible due to the higher enthalpy freestream flow, however the N_2 mass fraction only varies approximately 9% from its freestream value. Similar contours are shown in Figure 4 for a downstream region of the cone.

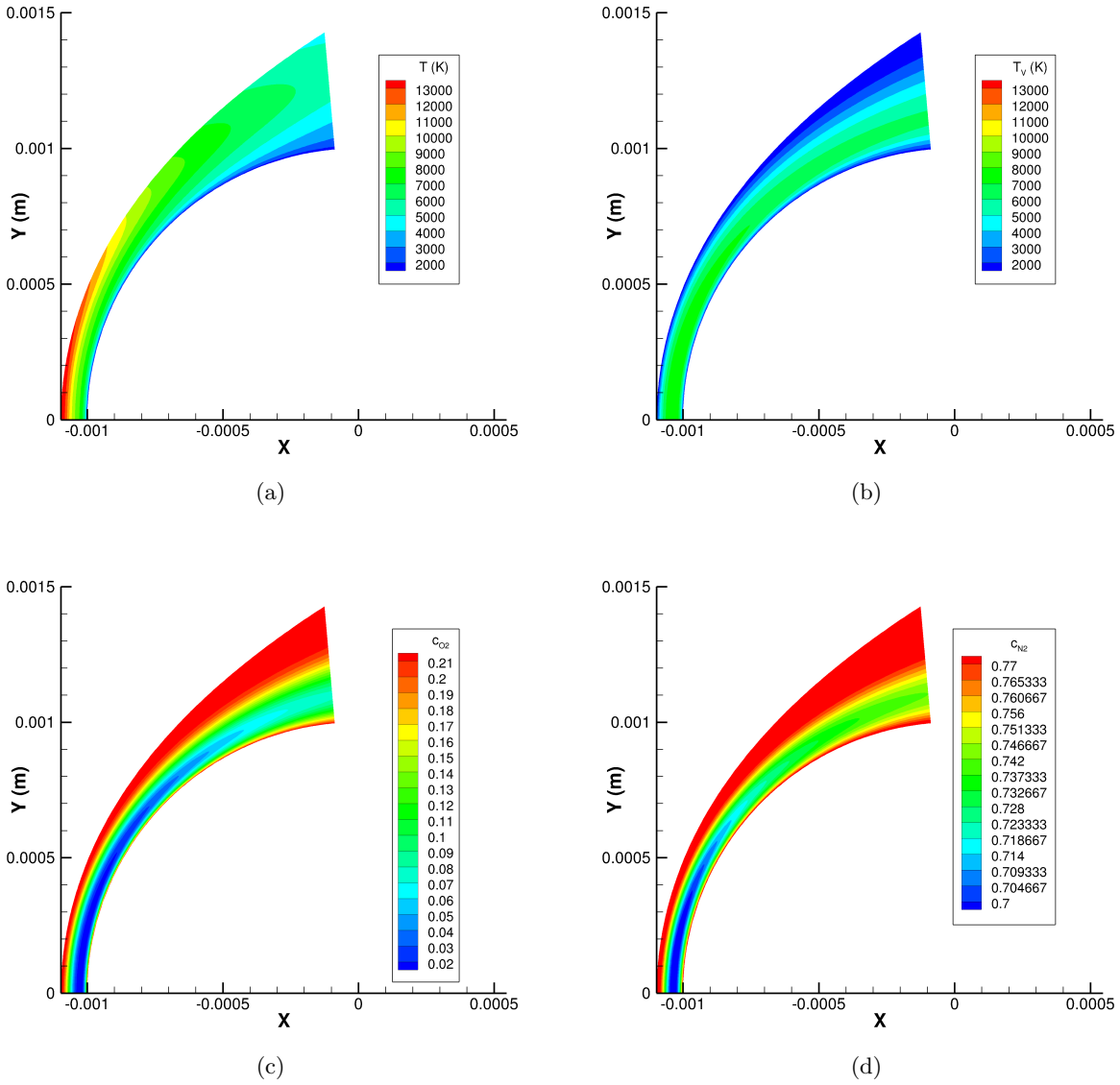

Figure 3: Steady DNS contours in nose region. (a) T. (b) T_V. (c) Mass fraction of O_2. (d) Mass fraction of N_2.

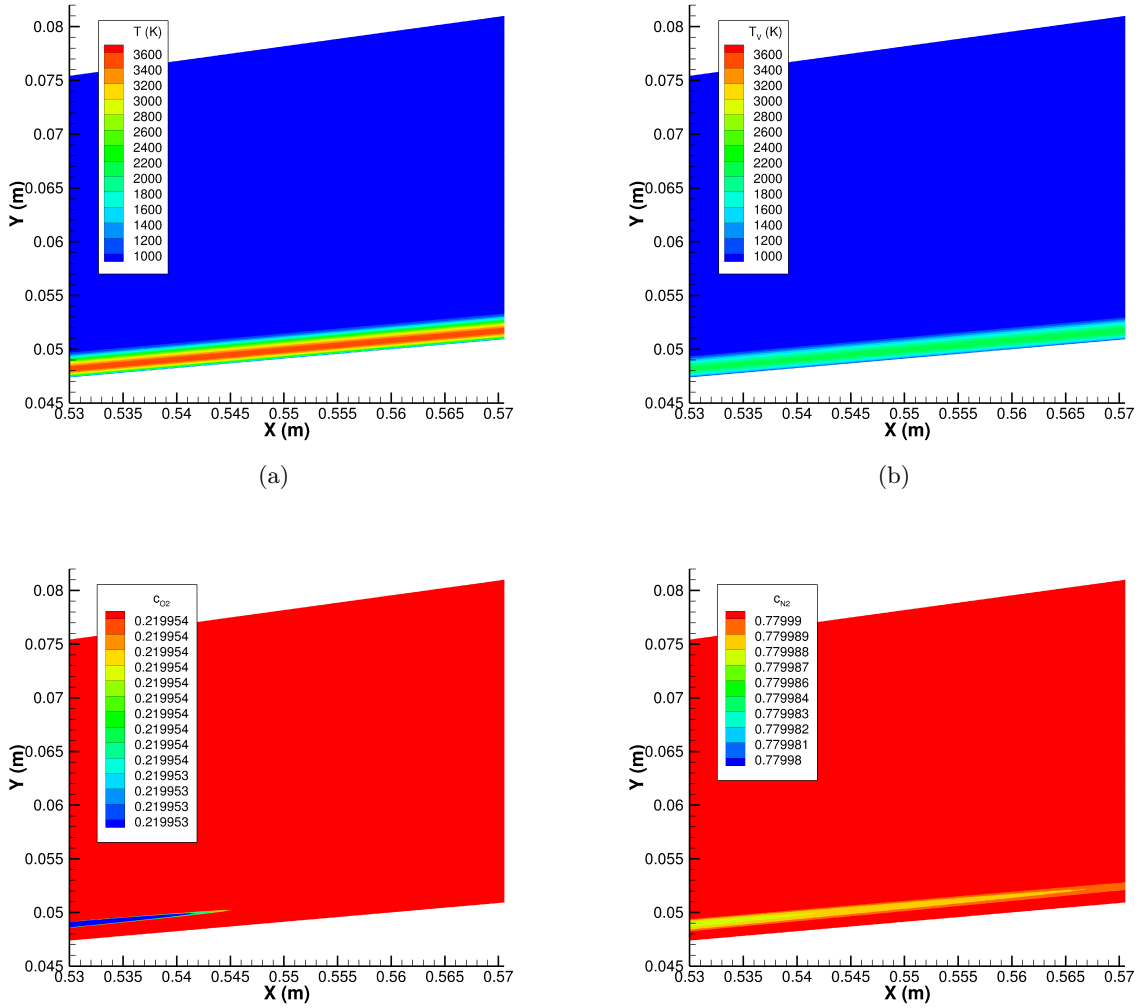

(a) (b)

(c) (d)

Figure 4: Steady DNS contours in a downstream region. (a) T. (b) T_V. (c) Mass fraction of O_2. (d) Mass fraction of N_2.

The thermal and chemical nonequilibrium is visible from the contours in Figure 4, however the meanflow profiles in Figure 5 show the nonequilibrium effects more clearly. The boundary layer profiles for temperature, vibration temperature, tangential velocity, and species density of N_2 and O_2 at a streamwise distance from the stagnation point of $s = 0.4$ m are shown in Figure 5. Again, y denotes the wall-normal distance. The meanflow does not reach thermal equilibrium in the free stream, thus demonstrating the necessity of accounting for the vibrational mode in these types of flows. The species densities of N_2 and O_2 follow similar trends to one another in the boundary layer, but ρ_{N2} specifically does not reach a constant value outside of the boundary layer. This demonstrates the need for simulations accounting for thermochemical nonequilibrium flows for high enthalpy freestream conditions.

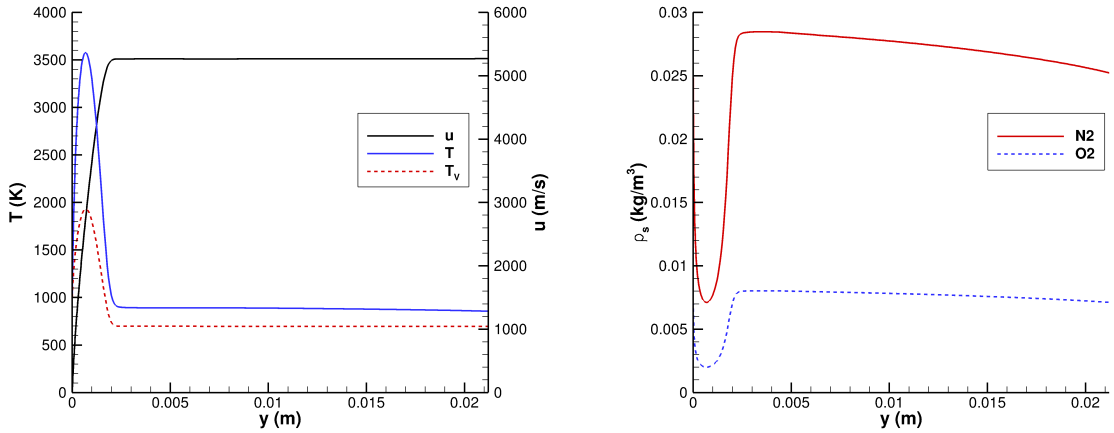

(a) (b)

Figure 5: Meanflow boundary layer profiles at $s = 0.4$ m. (a) u, T, and T_V. (b) Species density ρ_s of N_2 and O_2 species. u denotes the component of velocity tangential to the surface of the cone. y is the wall normal distance.

VI. LST Results

The freestream values used in nondimensionalizing the LST results were:

$$u^*_\infty = 5.303E+03 \text{ m/s}, \quad \rho^*_\infty = 1.991E-02 \text{ kg/m}^3, \quad \mu^*_\infty = 3.320E-05 \text{ kg m/s}.$$

The growth rate and phase speed for a frequency of $f = 1$ MHz is shown in Figure 6. These results indicate that mode S is unstable, rather than mode F1. The necessary condition for the supersonic modes is an unstable mode F1 with phase speed $c_r < 1 - 1/M_\infty$. Because mode S is the unstable mode, the supersonic mode will not exist under these flow conditions. The discontinuity in mode F1 in Figure 6 is a result of mode F1 synchronizing with the entropy/vorticity spectra and getting "lost" numerically. Because mode F1 is stable during synchronization with the entropy/vorticity spectra at $c_r = 1$, it is difficult to distinguish the discrete eigenvalues from the continuous eigenvalues, and the numerical scheme cannot converge to a single solution within any reasonable tolerance. More detail on the interaction between the discrete and continuous modes can be found in Fedorov.[2] To show unequivocally that mode S is unstable and mode F is stable, similar growth rate and phase speed results are presented in Figure 7 for a frequency of $f = 600$ kHz.

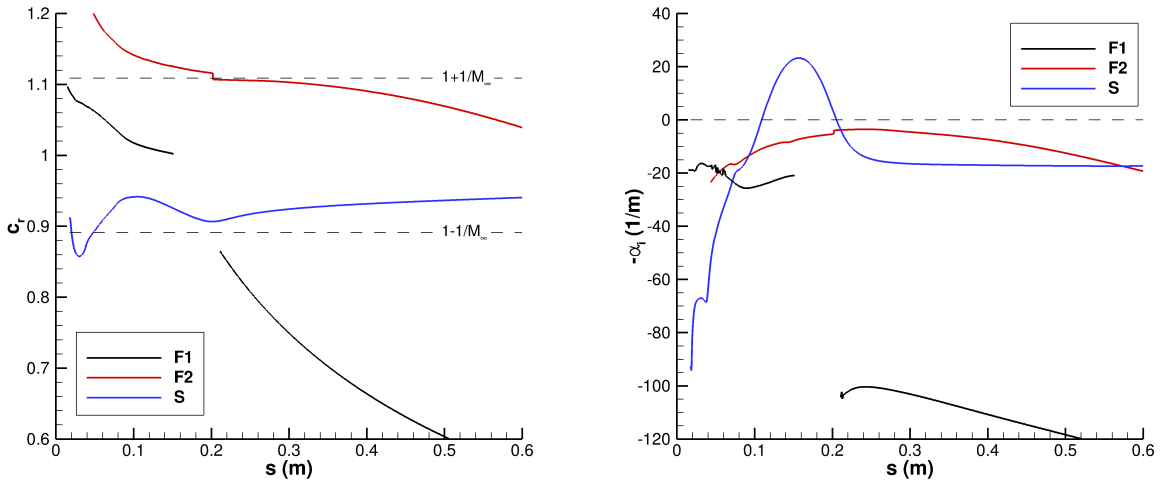

(a) (b)

Figure 6: LST phase speed and growth rate for Modes F1, F2, and S at $f = 1$ MHz. (a) Phase Speed. (b) Growth Rate.

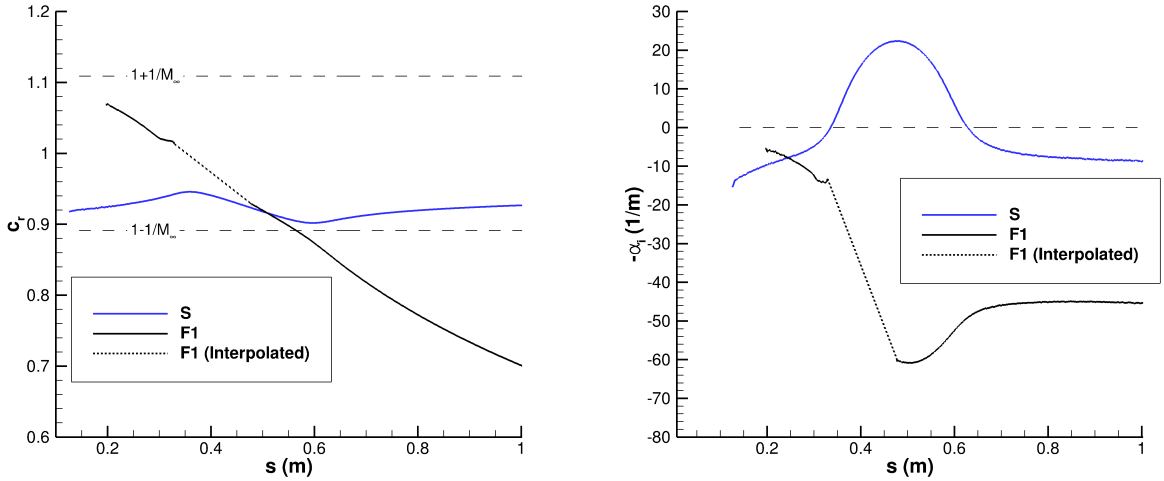

(a) (b)

Figure 7: LST phase speed and growth rate for Modes F1, F2, and S at $f = 600$ kHz. (a) Phase Speed. (b) Growth Rate.

The stability results for $f = 600$ kHz (Figure 7) also indicate mode S as the unstable mode. Mode F1 is not able to be resolved in the vicinity of $c_r = 1$ for the $f = 600$ kHz stability analysis (Figure 7) for the same reasoning as the $f = 1$ MHz analysis. However, from the linear interpolation across the entropy/vorticity spectra, it is reasonable to assume that mode F1 will be stable throughout the synchronization region. In any case, mode F1 is stable for $c_r < 1 - 1/M_\infty$, and no supersonic mode exists.

For a complete picture of the second mode, the stability of mode S for a range of frequencies over the entire length of the cone was computed, resulting in the neutral stability map for mode S (Figure 8). The neutral stability map indicates the locations and frequencies at which mode S is unstable. The region of instability of the second mode is the area inside the thick black curve. At the lowest frequencies and near the

nose of the cone (left-hand side of Figure 8), the numerical solver is not stable and a physical solution is not obtained. The maximum growth rate occurs at approximately $s = 0.24$ m at a frequency of $f = 840$ kHz. Because mode S is the unstable mode for these conditions, there can exist higher modes that are amplified. Specifically, the third mode amplification is apparent in the upper right corner of Figure 8. The third mode is amplified after the synchronization of mode F2 with mode S, however this amplification is not sufficient to make the third mode unstable. The second mode is significantly more amplified, and is the predicted cause of transition.

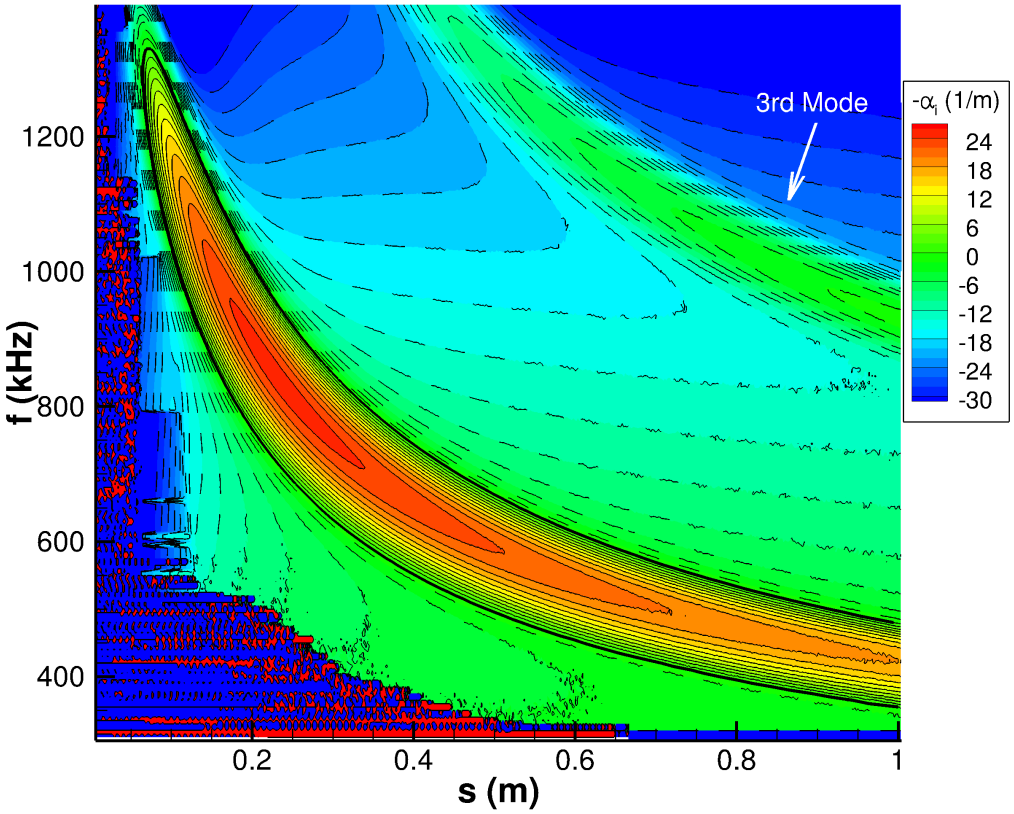

Figure 8: Neutral stability map for mode S. Dashed lines indicate negative growth rates. Thick black line indicates points of neutral stability.

To relate the mode S instability to empirical estimates of transition to turbulence, the N-factor curve was calculated, shown in Figure 9. A maximum N-factor of approximately 6 due to a frequency of $f = 475$ kHz is achieved by the end of the 1 m long cone.

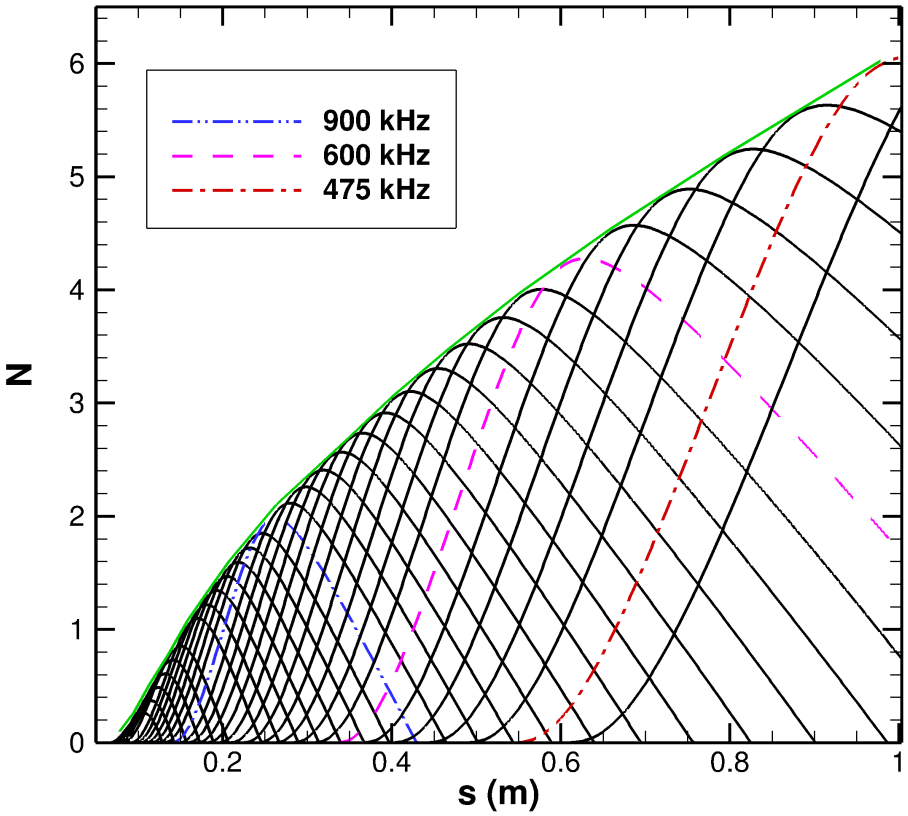

Figure 9: N-factor for unstable second mode frequencies. Frequencies are in increments of $\Delta f = 25$ kHz. The green line is an approximation of the edge of the N-factor curve.

VII. Unsteady DNS Results

To study stability using DNS, it is required that the meanflow be perturbed in order to study the growth, or decay, of the perturbation. Here, the flow is perturbed with a suction/blowing slot at the cone surface. The equation for the mass flux of the slot is

$$\rho v(x,t)'_w = \epsilon_b (\rho u)_\infty \exp\left\{-\frac{(t-\mu_b)}{2\sigma_b^2}\right\} \sin\left\{\frac{2\pi(x-x_b)}{l_b}\right\} \tag{31}$$

where l_b is the length of the slot, x_b is the center of the slot measured from the leading edge of the cone, ϵ_b scales the function, μ_b shifts the Gaussian component to avoid negative times, and σ_b adjusts the spectral content of the function. Notice the time dependent Gaussian portion of the function. When transformed to frequency space, this yields a continuous range of frequencies with non-zero amplitudes making this particular approach for perturbing the meanflow an effective strategy when studying a wide range of frequencies.

The parameters for the unsteady pulse, given by Equation 31, are summarized in Table 2. The Gaussian pulse and its Fourier transform (Figure 10) show the majority of the frequency content of the pulse is below 1.2 MHz.

Table 2: Gaussian pulse parameters for unsteady DNS

ϵ_b	μ_b	σ_b	x_b	l_b
$1E-4$	$3E-6$	$3E-7$	$0.1m$	$0.002m$

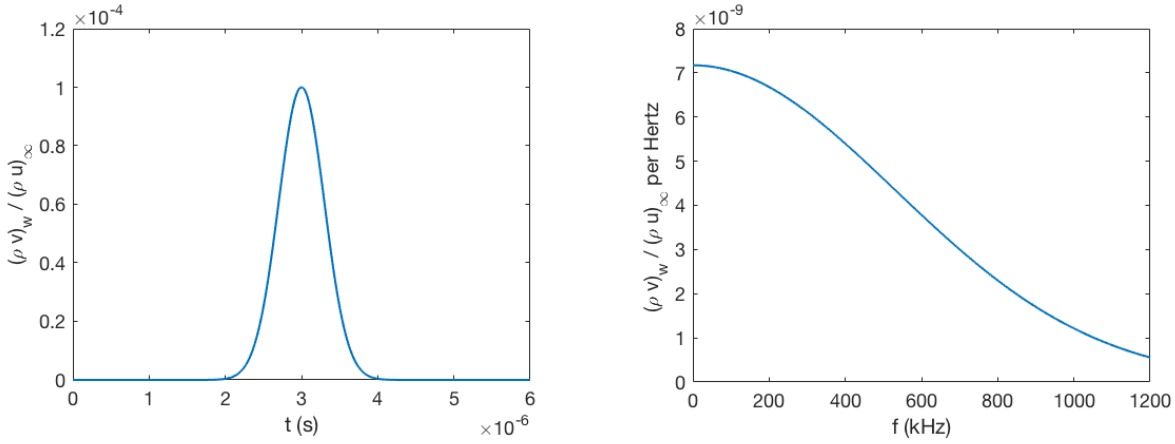

(a) (b)

Figure 10: Gaussian pulse for unsteady DNS. (a) Nondimensional mass flux amplitude. (b) Frequency content of pulse.

The evolution of the Gaussian pulse downstream is visualized in Figure 11 using snapshots in time of contours of the pressure perturbation normalized by the local meanflow pressure ($\frac{\Delta p}{p}$). The same value at the surface of the cone is included to more clearly visualize the growth of disturbances. The traditional second mode growth can be seen in Figure 11(a) prior to $x = 0.27$ m. However, contrary to the LST predictions, the start of the spontaneous radiation of sound appears in Figure 11(b) between $x = 0.30$ m and $x = 0.33$ m. When the pulse travels farther downstream, the spontaneous radiation of sound becomes much more apparent, shown in Figure 11(c-d). The radiation continues to grow into the freestream as the pulse continues downstream (Figure 12). Figure 12(b) in particular shows the sound radiation very clearly between $x = 0.73$ m and $x = 0.87$ m. Further Fourier decomposition analysis is required to determine whether or not this sound radiation is an artifact of the supersonic mode, or is due to other modal interaction.

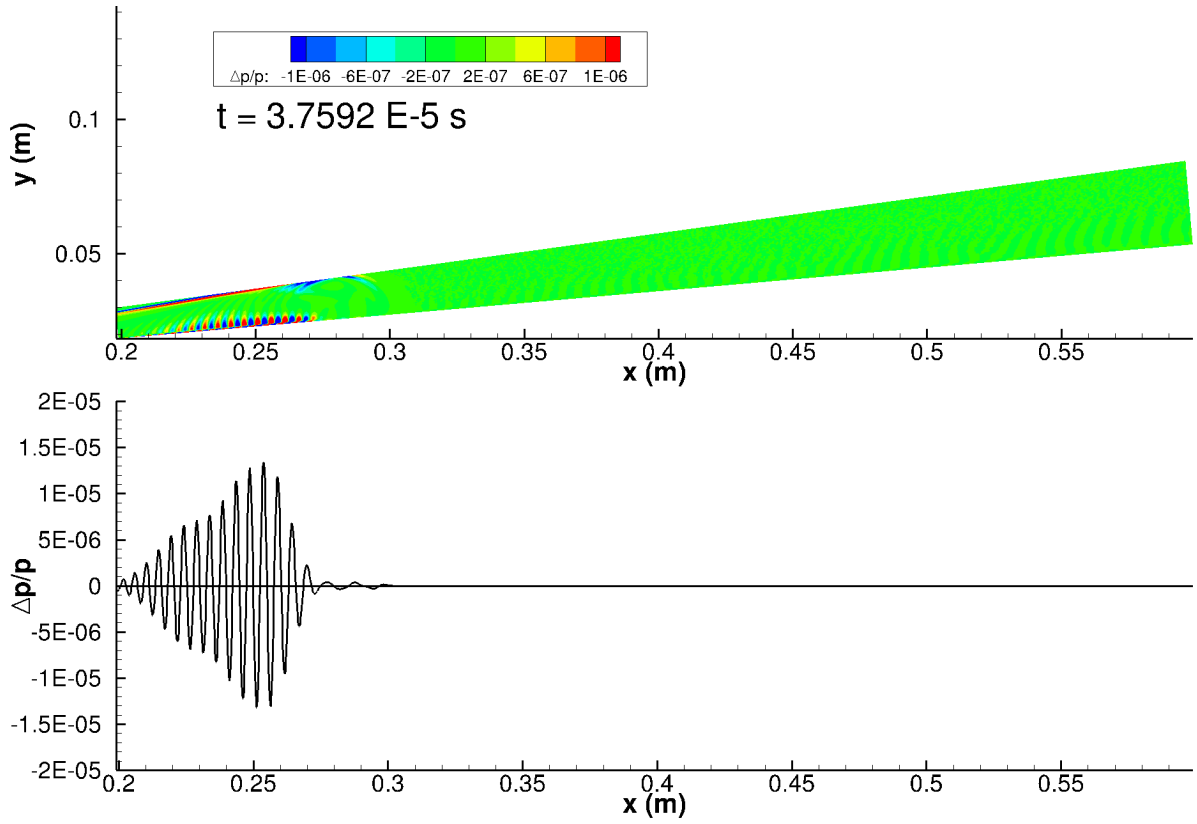
Δp/p: -1E-06 -6E-07 -2E-07 2E-07 6E-07 1E-06
t = 3.7592 E-5 s
y (m)
0.1
0.05
0.2
0.25
0.3
0.35
0.4
0.45
0.5
0.55
x (m)
2E-05
1.5E-05
1E-05
5E-06
0
-5E-06
-1E-05
-1.5E-05
-2E-05
Δp/p
x (m)

(a)

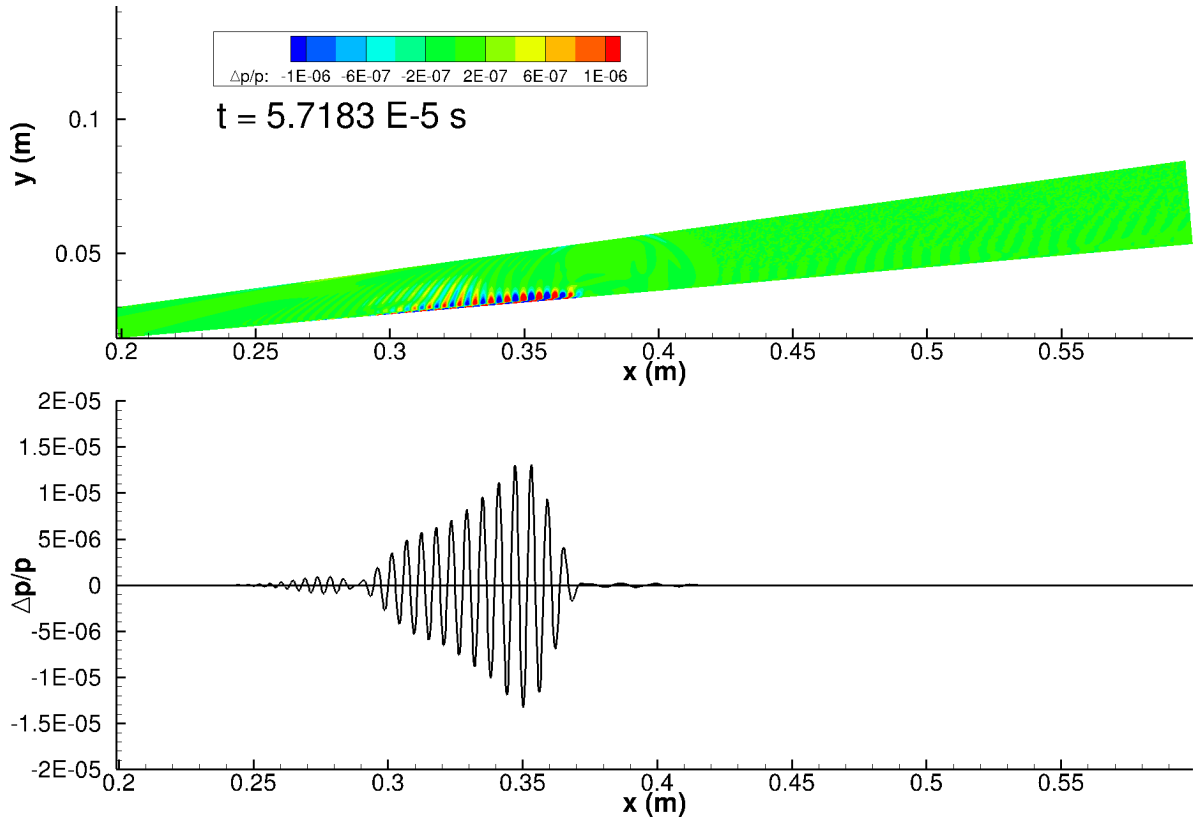
Δp/p: -1E-06 -6E-07 -2E-07 2E-07 6E-07 1E-06
t = 5.7183 E-5 s
y (m)
0.1
0.05
0.2
0.25
0.3
0.35
0.4
0.45
0.5
0.55
x (m)
2E-05
1.5E-05
1E-05
5E-06
0
-5E-06
-1E-05
-1.5E-05
-2E-05
Δp/p
x (m)

(b)

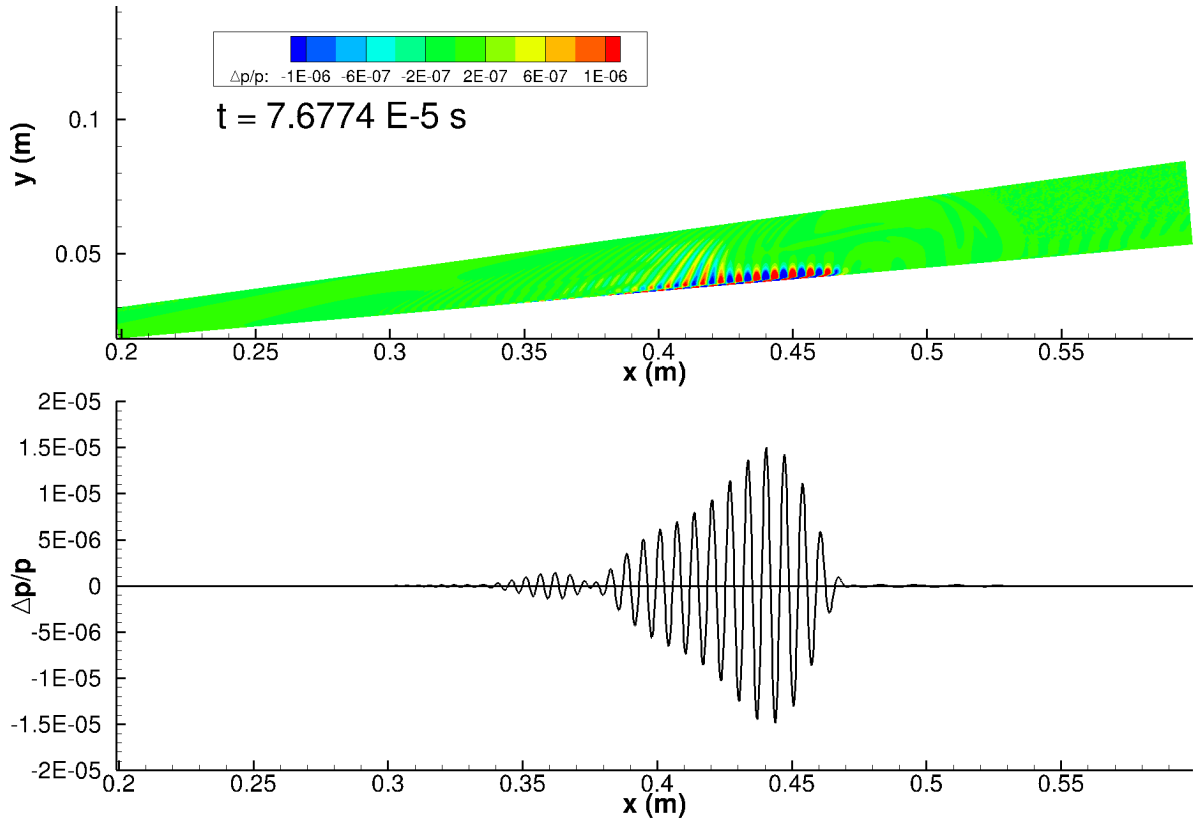

(c)

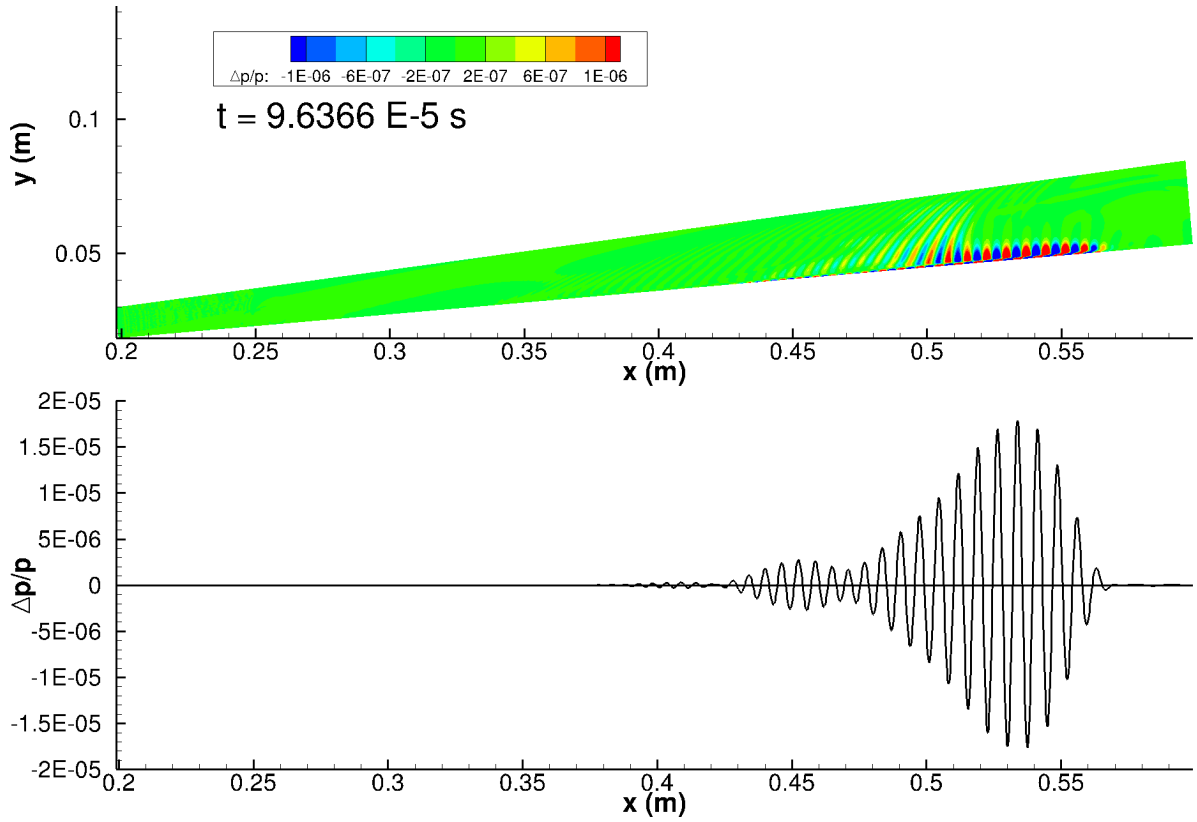

(d)

Figure 11: Snapshots in time of pressure perturbation $\Delta p/p$ contours and surface pressure perturbation from Gaussian pulse. Δt = 1.959 E-5 seconds.

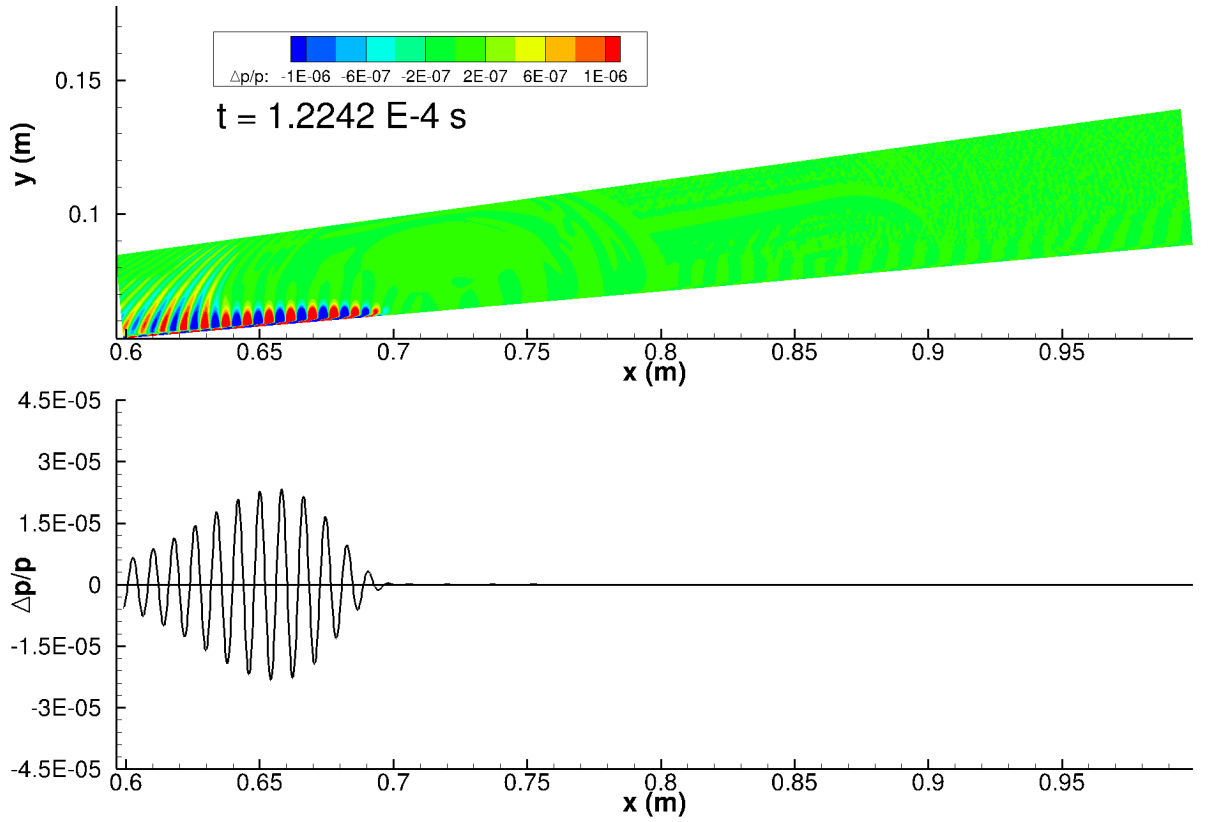
Δp/p: -1E-06 -6E-07 -2E-07 2E-07 6E-07 1E-06
t = 1.2242 E-4 s
y (m)
0.15
0.1
0.6
0.65
0.7
0.75
0.8
0.85
0.9
0.95
x (m)
4.5E-05
3E-05
1.5E-05
0
-1.5E-05
-3E-05
-4.5E-05
Δp/p
x (m)

(a)

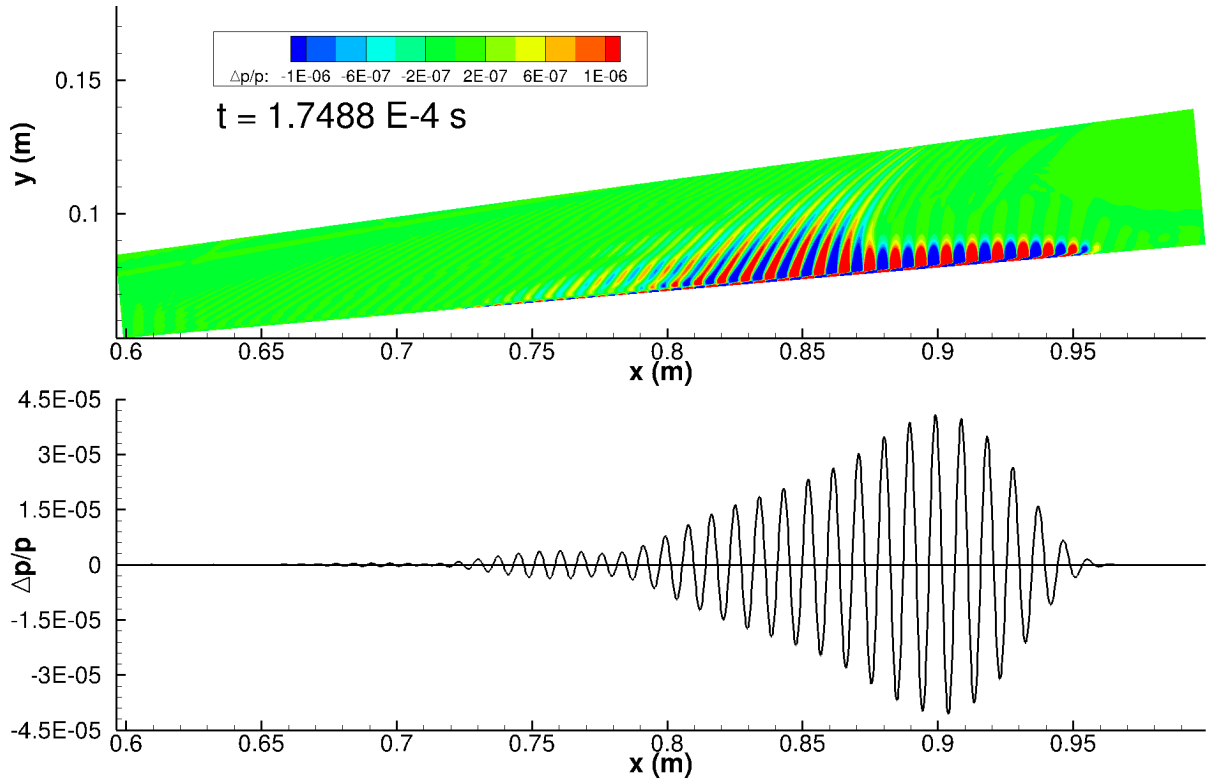
Δp/p: -1E-06 -6E-07 -2E-07 2E-07 6E-07 1E-06
t = 1.7488 E-4 s
y (m)
0.15
0.1
0.6
0.65
0.7
0.75
0.8
0.85
0.9
0.95
x (m)
4.5E-05
3E-05
1.5E-05
0
-1.5E-05
-3E-05
-4.5E-05
Δp/p
x (m)

(b)

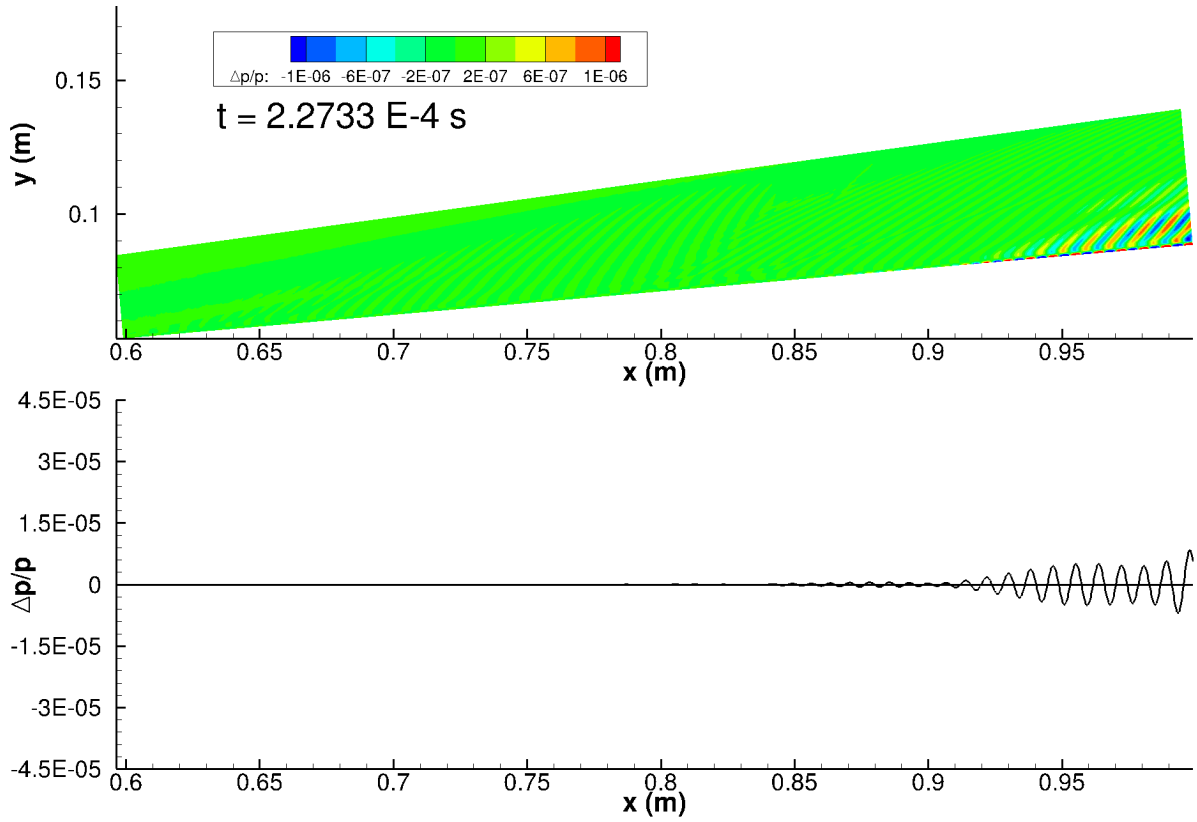

(c)

Figure 12: Snapshots in time of pressure perturbation $\Delta p/p$ contours and surface pressure perturbation from Gaussian pulse. Δt = 5.246 E-5 seconds.

An FFT was performed on the time-history of the surface pressure perturbation at all streamwise locations, resulting in the contour map in Figure 13. This contour shows the most unstable excited frequencies due to the Gaussian pulse. The neutral stability curve predicted by LST from Figure 8 is overlayed in Figure 13 for comparison.The most amplified frequency from the Gaussian pulse is approximately $f = 475$ kHz and appears most prominently for $s > 0.95$ m. This result agrees remarkably well the the N-factor results from LST. The FFT results follow the LST predictions reasonably closely despite the absence of the radiation of sound in the LST results. It is likely that the amplitude of the supersonic mode is relatively weak in this flow, and the traditional 2nd mode is the dominant instability.

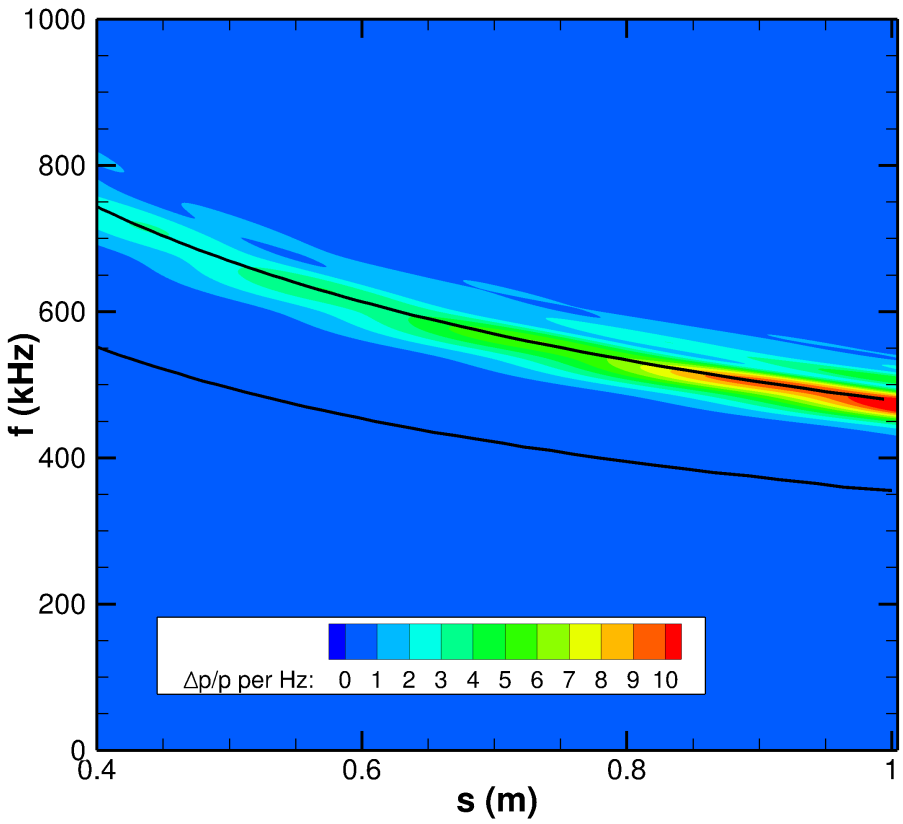

Figure 13: Fourier transform of unsteady surface pressure perturbation time history of Gaussian pulse. The black line is the neutral curve predicted by LST.

It is useful to compare the FFT results to those obtained by Chuvakhov and Fedorov[15] for a cold-wall flat plate. Although the wall temperature ratio and blowing/suction slot are different than the current study, similar trends are observed for their supersonic mode. The Fourier transform of the unsteady pressure perturbation vs frequency for fixed streamwise locations is shown in Figure 14. Near the blowing/suction actuator ($s \leq 0.201$ m), the curve shape is similar to a bell curve. However, as the pulse travels downstream, the frequency content shifts and becomes asymmetrical. At each location $s \geq 0.250 = 2$ m, there is a main peak frequency with at least one smaller peak frequency greater than that main frequency. Chuvakhov and Fedorov[15] also obtained similar results for their study, in which they noted that rather than the typical bell-shaped curves, multiple peaks are formed. Chuvakhov and Fedorov[15] observed three peaks at most in their FFT, which largely agrees with the results presented in Figure 14.

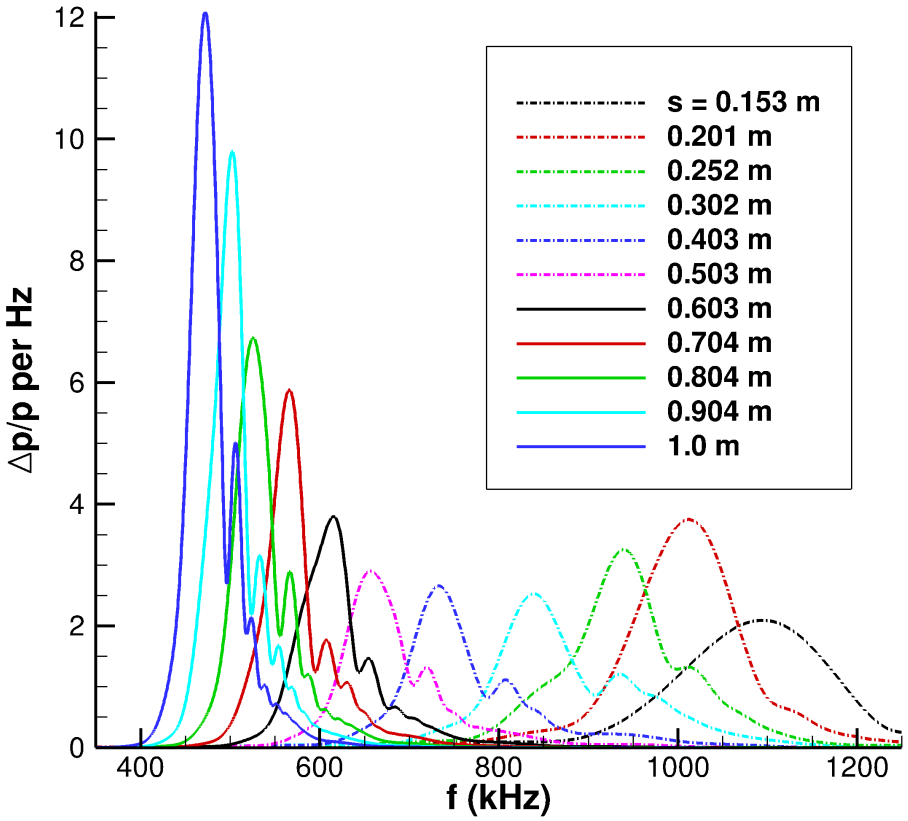

Figure 14: Fourier transform of unsteady surface pressure perturbation time history of Gaussian pulse as a function of frequency for various streamwise locations s.

It is possible to determine the growth rate and phase speed of an unsteady disturbance in DNS. The Fourier decomposed perturbation variables can be used to reconstruct the perturbation flow field via

$$\phi'(x, y, t) = \Delta\phi(x, y) \exp\left[i(\psi(x, y) - 2\pi f t)\right] \tag{32}$$

where ϕ' is the perturbation of some variable, $\Delta\phi$ is the amplitude of that variable, ψ is the corresponding phase angle, and f represents a single dimensional frequency. The response of the entire flow field for a particular frequency as a result of the unsteady pulse can be given directly by Equation 32, provided FFT data is available for all data points in the flow field.

The FFT of the entire flow field was performed and is shown in Figure 15 for 500 kHz and Figure 16 for 700 kHz. Both frequencies clearly show the extension of the disturbance outside of the boundary layer, which is typical of the supersonic mode. The onset of the radiation into the freestream for $f = 500$ kHz is near $x = 0.7$ m, and for $f = 700$ kHz the onset is near $x = 0.35$ m. For the $f = 700$ kHz frequency, there is a clear amplification in the freestream for $x > 0.7$ m while there is very little amplification near the wall in this region.

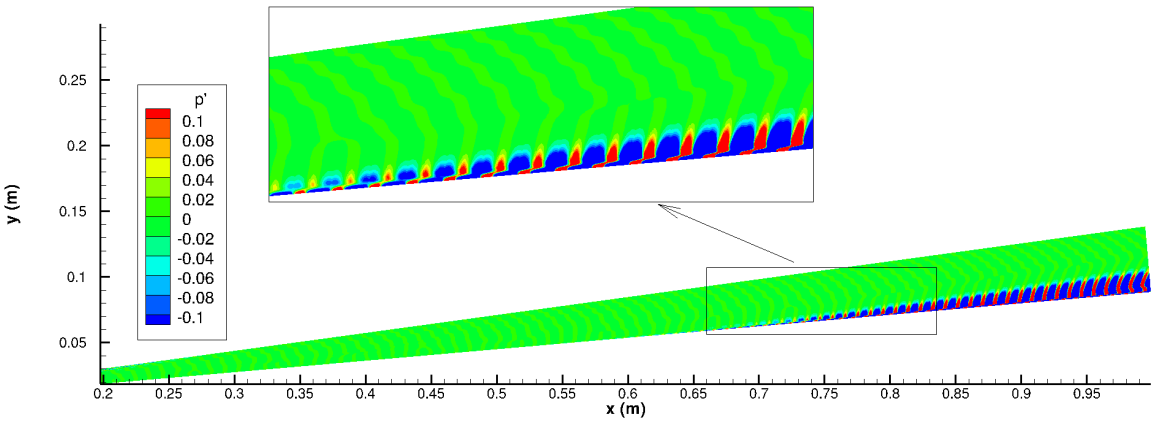

Figure 15: FFT of unsteady pressure perturbation at all points in the flow field for $f = 500$ kHz.

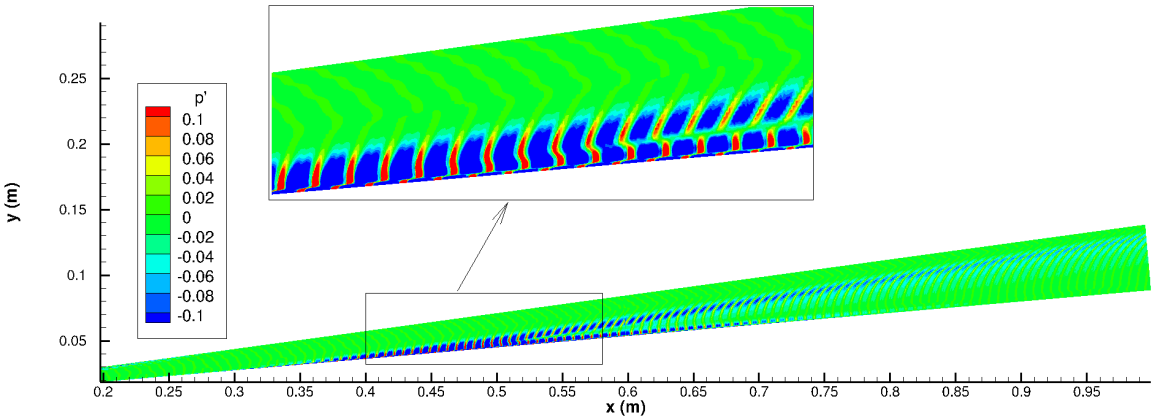

Figure 16: FFT of unsteady pressure perturbation at all points in the flow field for $f = 700$ kHz.

Multiple boundary layer modes are present simultaneously in DNS, however as one mode becomes dominant, it is possible to derive growth rate, wave number, and phase speed equations for a given frequency f from Equation 32, resulting in

$$-\alpha_i = \frac{1}{\Delta\phi(f)} \frac{d}{ds} \Delta\phi(f) \tag{33}$$

$$\alpha_r = \frac{d}{ds} \psi(f) \tag{34}$$

$$c_r = \frac{2\pi f}{\alpha_r} \tag{35}$$

$$\tag{36}$$

where s is the streamwise coordinate, $\Delta\phi(f)$ represents a variable amplitude frequency f, and $\psi(f)$ represents the corresponding phase angle at frequency f. Similar to previous researchers,[52] the surface pressure perturbations from DNS are used to compute $-\alpha_i$ and c_r.

The phase speed and growth rate calculated from DNS is compared to the LST predictions for a frequency of $f = 500$ kHz in Figure 17, and for $f = 700$ kHz in Figure 18. The DNS matches the LST predictions reasonably well, with a few areas of exception. For $f = 500$ kHz, the phase speed for DNS and LST agree closest in the range $0.6 < s < 0.85$ m, although the DNS phase speed is consistently lower than the LST prediction. The growth rate is also closest in this range, and the DNS growth rate is consistently greater than the LST predictions. The areas where the agreement is not as strong are $s < 0.6$ m and $s > 0.85$ m. These regions correspond to synchronization regions with the fast acoustic mode F1 and the slow acoustic

spectra, respectively. The DNS results are a combination of all discrete and continuous modes present in the flow, whereas the LST results focus on a single mode and neglect all other modes. In regions where there are competing modes, LST is unable to capture the interaction between these modes, whereas DNS exhibits the oscillatory behavior due to the interaction between modes.

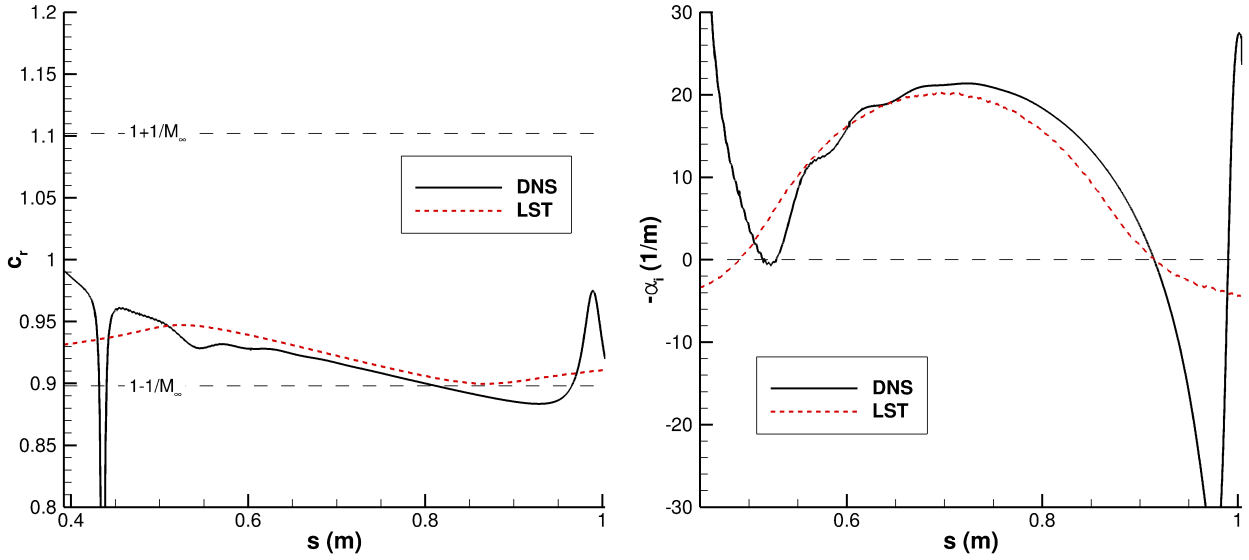

(a) (b)

Figure 17: Comparison of DNS to LST phase speed and growth rate at $f = 500$ kHz. (a) Phase speed, c_r. (b) Growth rate, $-\alpha_i$.

The phase speed and growth rate for $f = 700$ kHz in Figure 18 draw largely similar comparisons as the $f = 500$ kHz results. The stable boundary layer modes F1 and F2 are also included for comparison. There are a few notable differences compared to the 500 kHz case, however. The region of mode S between the interaction with mode F1 and the slow acoustic spectrum is $0.3 < s < 0.45$ m, and the DNS and LST mode S results are similar, although the DNS phase speed is slower than predicted by LST, and the DNS growth rate is larger than predicted by LST. Downstream of $s = 0.45$ m, the DNS results oscillate about the LST mode S predictions for both phase speed and growth rate. Again, this oscillatory behavior is the result of multiple modes existing simultaneously in the DNS simulation that are ignored in LST. However, the agreement between DNS and LST is still strong considering the largely different methods used to obtain the results.

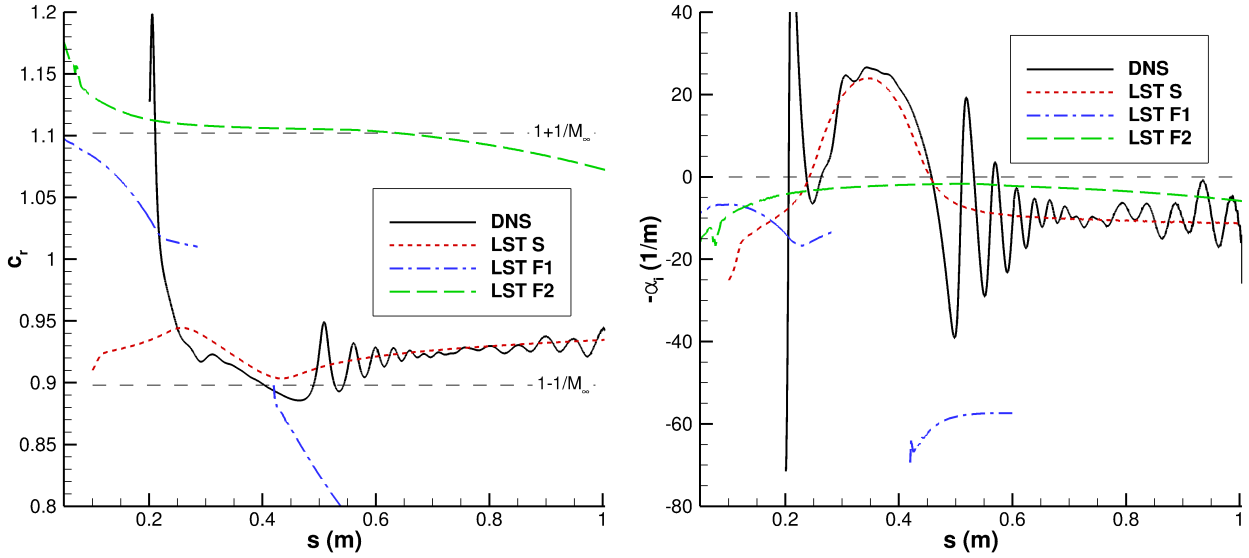

(a) (b)

Figure 18: Comparison of DNS to LST phase speed and growth rate at $f = 700$ kHz. (a) Phase speed, c_r. (b) Growth rate, $-\alpha_i$.

From the growth rate and phase speed comparison between DNS and LST, it appears that the DNS phase speed is below $1 - 1/M_\infty$ in some cases, which is the key requirement of the supersonic mode. The eigenfunctions between LST and DNS can be compared to determine to what extent there is oscillatory behavior in the freestream at these locations, indicating the presence of the supersonic mode. Figure 19 compares the pressure eigenfunctions from LST mode S and DNS at three streamwise locations for $f = 500$ kHz. At $s = 0.6$ m, mode S has just synchronized with mode F1 and the DNS eigenfunction exhibits some oscillatory behavior in the freestream, although the amplitude is quite small. This oscillatory behavior in the freestream is distinct from the supersonic mode because the phase speed of the disturbance is greater than $1 - 1/M_\infty$. Further downstream at $s = 0.7$ m, the effects of the interaction between modes S and F1 are much smaller and the DNS and LST eigenfunctions are nearly identical. The LST growth rate in Figure 17(b) predicts mode S to be dominant at $s = 0.7$ m, so the good agreement between DNS and LST was expected at this location. At $s = 0.9$ m, it appears from Figure 17(a) that the DNS phase speed may be supersonic ($c_r < 1 - 1/M_\infty$). However, the pressure eigenfunction in 19(c) does not show any oscillatory behavior in the freestream, so the extension of the disturbance into the freestream in the FFT contour in Figure 15 is not due to a supersonic mode S. Rather it is likely due to the interaction of mode S, mode F1, and the slow acoustic spectrum.

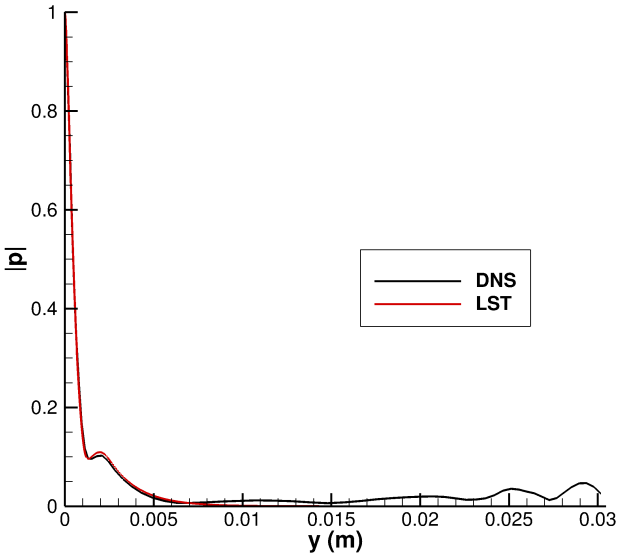

(a) $s = 0.6$ m

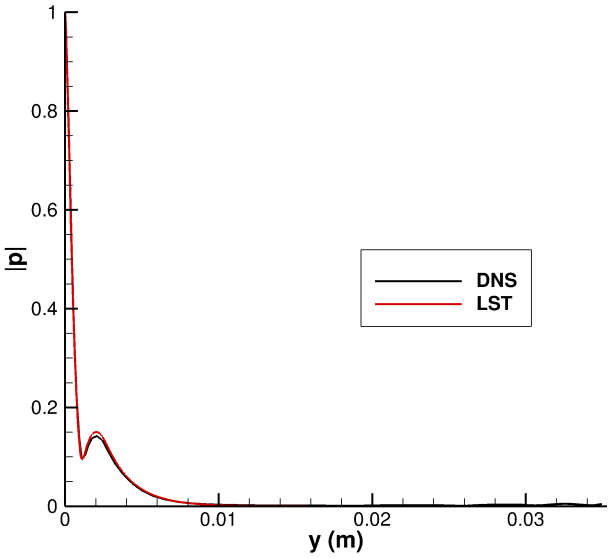

(b) $s = 0.7$ m

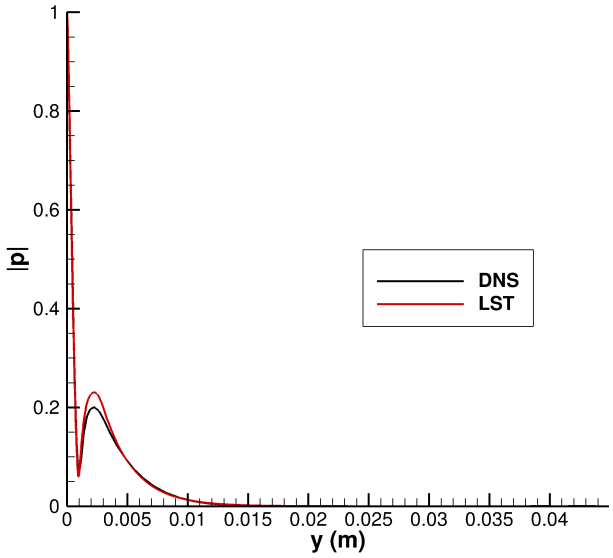

(c) $s = 0.9$ m

Figure 19: Comparison of DNS to LST mode S pressure eigenfunction at $f = 500$ kHz at different streamwise locations.

The eigenfunctions at $f = 700$ kHz were also compared to the LST mode S, mode F1, and mode F2 predictions at different streamwise locations, shown in Figure 20. Similar to the 500 kHz cases, locations for eigenfunction comparison were selected to be just downstream of the synchronization of mode S with mode F1 ($s = 0.35$ m), and in the region where $c_r < 1 - 1/M_\infty$ ($s = 0.45$ m). The third location was selected based on Figure 16 where there are two distinct wall-normal locations of amplification ($s = 0.6$ m). At $s = 0.35$ m, the synchronization of mode S with mode F1 causes small oscillatory behavior in the freestream, although the amplitude is very small. At $s = 0.45$ m, the DNS phase speed is supersonic ($c_r < 1 - 1/M_\infty$), however the DNS and LST mode S eigenfunctions do not exhibit any oscillatory behavior outside the boundary layer. Mode F1, however, exhibits strongly oscillatory behavior in the freestream due to its proximity to the slow acoustic spectrum, but nevertheless it is predicted to be stable. Because mode F1 was not able to be

resolved between $0.3 < s < 0.4$ m, it is possible that the interaction of the unstable mode S, stable mode F1, and the slow acoustic spectrum cause mode F1 to be briefly unstable while traveling supersonically with respect to the freestream. This could explain the brief radiation of sound shown in Figure 16. At $s = 0.45$ m, the mode S and DNS growth rates are near zero, and no significant unstable supersonic mode S exists. Interestingly, however, the eigenfunction at $s = 0.6$ m displays a clear second peak that is not predicted by LST despite a subsonic phase speed and a negative growth rate. It is possible that this behavior in DNS is the result of the brief radiation of sound upstream of this location. In other words, it is likely that somewhere between $0.3 < s < 0.4$ m there is a modal energy exchange causing mode F1 to become briefly unstable while traveling supersonically with respect to the meanflow. This briefly unstable supersonic mode radiates sound away from the wall. The sound radiation outside of the boundary layer continues to travel downstream and its amplitude becomes slowly damped. Near the wall, however, the supersonic mode F1 becomes stable very quickly after its creation, and mode S becomes stable as well. This scenario would explain the sound radiation in the freestream and the decay of the perturbation at the wall observed in Figure 16. This type of modal interaction is indeed very similar to the creation of the supersonic mode, however it is not predicted by LST because of the assumption that each mode acts independently. In the creation of the supersonic mode, the discrete mode undergoes significant modulation and can be predicted by LST. However, when the discrete mode S is not affected significantly by the slow acoustic spectrum, and mode F1 is not able to be resolved as it is in this case, it is not possible to determine accurate stability predictions with traditional LST solvers. Therefore, because the supersonic mode in this flow is the result of the interaction of modes, it is not expected that the radiation of sound will be apparent in the LST results. To investigate the relative contribution of each mode to the DNS disturbance, a multimode decomposition using methods and tools developed by Gaydos and Tumin[53] and Miselis, Huang, and Zhong[54] must be performed.

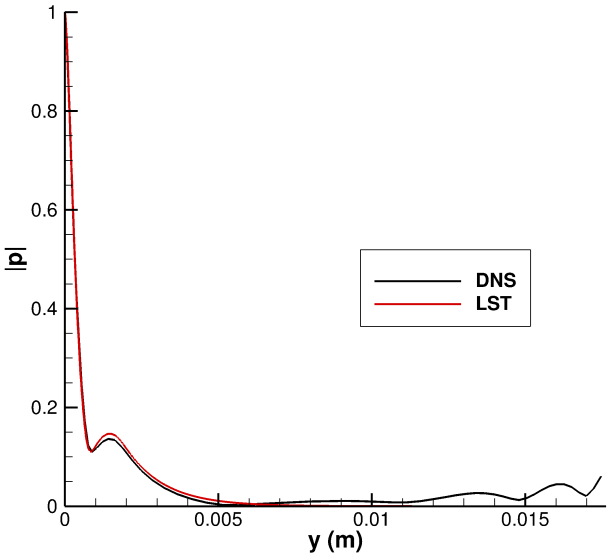

(a) $s = 0.35$ m

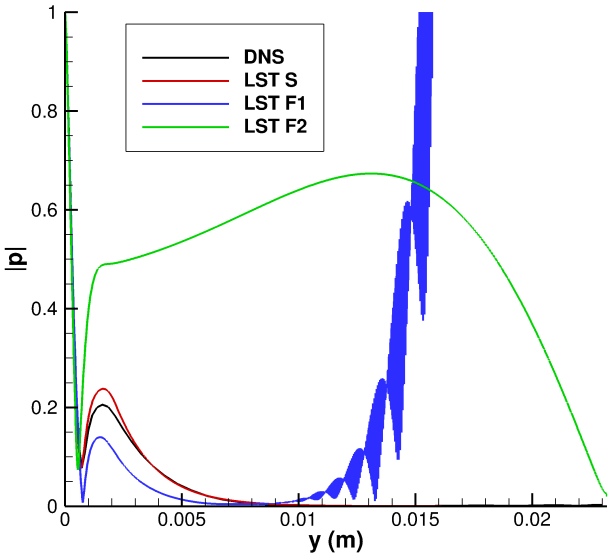

(b) $s = 0.45$ m

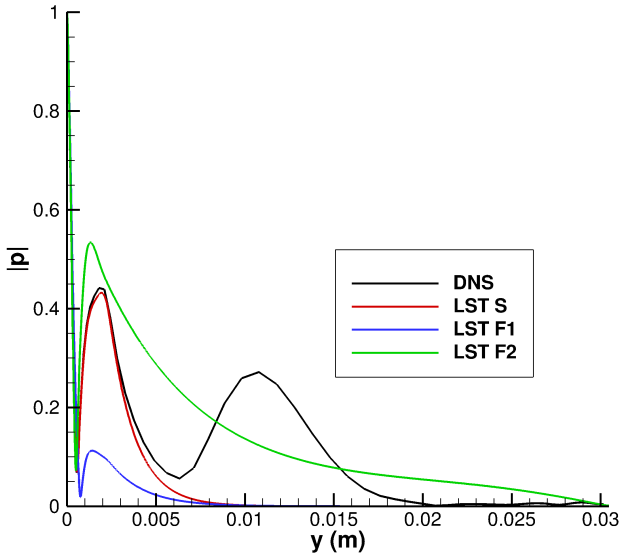

(c) $s = 0.6$ m

Figure 20: Comparison of DNS to LST pressure eigenfunction at $f = 700$ kHz at different streamwise locations.

Modal interactions have been examined in a number of circumstances. The interaction of the discrete mode S and mode F1 with the slow and fast acoustic spectra, respectively, near the leading edge of a flat plate has been examined by Fedorov and Khokhlov[55,56] using a mathematical model for the freestream acoustic waves exciting modes F1 and S. Later, Fedorov[57] noted acoustic disturbances near leading edge can transfer energy to the discrete boundary layer modes, inducing oscillatory behavior. The synchronization of mode F1 with the entropy/vorticity spectra was also analyzed by Fedorov and Khokhlov,[56] who found that oscillations in mode F1 can exist outside of the boundary layer near the synchronization location with the entropy/vorticity spectra. They found that mode F1 crossing entropy/vorticity spectra can cause mode F1 to become less stable (or even unstable), which eventually interacts with mode S, causing the second mode instability. Lastly, this synchronization between mode F1 and mode S has been modeled by Gushchin and

Fedorov[58] and later by Fedorov and Tumin,[59] indicating that the second mode instability is created by the energy exchange between mode F1 and mode S.

To date, there have been no investigations of the effects of tri-modal interactions (to the author's knowledge). It is indeed uncommon to encounter a synchronization between mode S, mode F1, and the slow acoustic spectrum as is the case in this study. However, the mathematical framework for such a study has already been laid out by Fedorov.[57] Studying a tri-modal interaction with the LST tool used here is not possible; rather similar tools used by Fedorov[57] are more appropriate. However, the most accurate method of determining the influence of each mode is to use a multimode decomposition technique similar to Gaydos and Tumin[53] or Miselis, Huang, and Zhong.[54] However, these tools currently assume a perfect gas model and would need to be altered to incorporate a thermochemical nonequilibrium model similar to the one used in this study.

The implications of the radiation of sound from the boundary layer into the freestream in this particular case are the same as for the longer-lasting supersonic mode observed by Knisely and Zhong.[16] However, because the supersonic mode in this case is relatively short-lived, it may not have as significant of an impact on the stability results. The sound radiation may act as an energy sink for the boundary layer disturbance,[15] and could affect stability prediction solvers such as LST. The presence of this sound radiation caused an abnormal dispersion of the frequency content of the disturbance as opposed to the traditional bell-shaped curve, which, as noted by Chuvakhov and Fedorov,[15] brings into question the applicability of the e^N method of transition prediction. Nevertheless, LST calculations applying the e^N method to flows with the spontaneous radiation of sound should be treated with caution, as it is likely that this tool will not resolve this physical artifact and may inaccurately predict the transition location.

VIII. Summary and Conclusions

The flow conditions considered here induced significant thermochemical nonequilibrium in the flow downstream of the stagnation point. The LST results indicate that mode S is the unstable mode for this case, and therefore no supersonic mode was expected to exist. This conclusion goes against the suggestion by Edwards and Tumin[32] that chemical nonequilibrium effects may be responsible for the supersonic mode. However, unsteady DNS results did indicate the presence of sound radiation away from the wall. Further FFT analysis indicated that this sound radiation was not due to a supersonic mode S directly, but was actually due to the interaction of mode S and mode F1 with the slow acoustic spectrum; a subtle but important distinction. The unstable mode S may interact with a stable mode F1 and the slow acoustic spectrum, causing the supersonic mode F1 to very briefly become unstable and radiate sound away from the boundary layer. Further downstream, both mode S and F1 are stable, but the sound radiation from the upstream interaction is still decaying as it travels downstream. Because mode S is stable and subsonic when this interaction occurs, and mode F1 was not distinguishable from the continuous spectra, most LST solvers will not predict the radiative behavior and could affect boundary layer transition prediction. The radiated sound from the wall may have an impact on the stability of the boundary layer, and it is possible the sound radiation acts as an energy sink for the 2nd mode, as suggested by Chuvakhov and Fedorov.[15] Transition prediction tools such as the e^N method should be used with caution when applied to hypersonic boundary layers with the spontaneous radiation of sound.

Acknowledgments

This research was supported by the U.S. Air Force Office of Scientific Research (AFOSR) through the National Defense Science & Engineering Graduate Fellowship (NDSEG) Program. Primary computational resources were provided by the AFOSR, USAF, under AFOSR Grant #FA9550-15-1-0268, monitored by Dr. Ivett Leyva. Additional computational resources were provided by Extreme Science and Engineering Discovery Environment (XSEDE) provided by Texas Advanced Computing Center (TACC) and San Diego Supercomputer Center (SDSC) under grant number TG-ASC090076, supported in part by the National Science Foundation. This research was also supported by Office of Naval Research (ONR) Grant #N00014-17-1-2343, monitored by Dr. Knox Millsaps. The views and conclusions contained herein are those of the authors and should not be interpreted as necessarily representing the official policies or endorsements, either expressed or implied, of the U.S. Air Force Office of Scientific Research, Office of Naval Research, or the U.S. Government.

References

[1]Mack, L. M., "Boundary Layer Linear Stability Theory," Tech. rep., AGARD report No. 709, 1984.

[2]Fedorov, A., "Transition and Stability of High-Speed Boundary Layers," *Annual Review of Fluid Mechanics*, Vol. 43, 2011, pp. 79–95.

[3]Malik, M. R., "Numerical Methods for Hypersonic Boundary Layer Stability," *Journal of Computational Physics*, Vol. 86, 1990, pp. 376–413.

[4]Stuckert, G. and Reed, H., "Linear Disturbances in Hypersonic, Chemically Reacting Shock Layers," *AIAA Journal*, Vol. 32, No. 7, 1994, pp. 1384–1393.

[5]Hudson, M. L., Chokani, N., and Candler, G., "Linear Stability of Hypersonic Flow in Thermochemical Nonequilibrium," *AIAA Journal*, Vol. 35, No. 6, 1997, pp. 958–964.

[6]Johnson, H. B., Seipp, T. G., and Candler, G., "Numerical study of hypersonic reacting boundary layer transition on cones," *Physics of Fluids*, Vol. 10, No. 10, 1998, pp. 2676–2685.

[7]Johnson, H. B. and Candler, G., "Hypersonic Boundary Layer Stability Analysis Using PSE-Chem," *AIAA 2005-5023*, 2005.

[8]Johnson, H. B. and Candler, G., "Analysis of Laminar-Turbulent Transition in Hypersonic Flight Using PSE-Chem," *AIAA 2006-3057*, 2006.

[9]Bitter, N. and Shepherd, J., "Stability of highly cooled hypervelocity boundary layers," *Journal of Fluid Mechanics*, Vol. 778, 2015, pp. 586–620.

[10]Sherman, M. M. and Nakamura, T., "Flight test measurements of boundary-layer transition on a nonablating 22 deg cone," *Journal of Spacecraft and Rockets*, Vol. 7, No. 2, 1970, pp. 137–142.

[11]Malik, M. R., "Hypersonic flight transition data analysis using parabolized stability equations with chemistry effects," *Journal of Spacecraft and Rockets*, Vol. 40, No. 3, 2003, pp. 332–344.

[12]Lees, L., "The Stability of the Laminar Boundary Layer in a Compressible Fluid," Tech. Rep. 876, NACA, 1947.

[13]Mack, L., "Review of Linear Compressible Stability Theory," *Stability of Time Dependent and Spatially Varying Flows*, edited by D. Dwoyer and M. Hussaini, Springer-Verlag, 1985, pp. 164–187.

[14]Mack, L., "Effect of cooling on boundary-layer stability at Mach number 3," *Instabilities and Turbulence in Engineering Flows*, edited by D. Ashpis, T. Gatski, and R. Hirsch, Springer-Verlag, 1993.

[15]Chuvakhov, P. and Fedorov, A., "Spontaneous radiation of sound by instability of a highly cooled hypersonic boundary layer," *8th AIAA Flow Control Conference*, , No. AIAA 2016-4245, 2016.

[16]Knisely, C. and Zhong, X., "An Investigation of Sound Radiation by Supersonic Unstable Modes in Hypersonic Boundary Layers," *AIAA 2017-4516*, 2017.

[17]Demetriades., A., "Hypersonic viscous flow over a slender cone; part iii: Laminar instability and transition." *AIAA 74-535*, 1974.

[18]Zhang, C.-H., Tang, Q., and Lee, C.-B., "Hypersonic boundary-layer transition on a flared cone," *Acta Mechanica Sinica*, Vol. 29, No. 1, 2013, pp. 48–53.

[19]Zhong, X. and Ma, Y., "Boundary-layer receptivity of Mach 7.99 flow over a blunt cone to free-stream acoustic waves," *Journal of Fluid Mechanics*, Vol. 556, 2006, pp. 55–103.

[20]Parsons, N., Zhong, X., Kim, J., and Eldredge, J., "Numerical Study of Hypersonic Receptivity with Thermochemical Non-Equilibrium on a Blunt Cone," *AIAA 2010-4446*, 2010.

[21]Heitmann, D. and Radespiel, R., "Simulation of the interaction of a laser generated shock wave with a hypersonic conical boundary layer," *AIAA 2011-3875*, 2011.

[22]Chang, C.-L., Vinh, H., and Malik, M., "Hypersonic Boundary-Layer Stability with Chemical Reactions using PSE," *28th AIAA Fluid Dynamics Conference, Snowmass Village, CO, U.S.A.*, 1997.

[23]Fedorov, A., Soudakov, V., and Leyva, I., "Stability analysis of high-speed boundary-layer flow with gas injection," *7th AIAA Theoretical Fluid Mechanics Conference*, , No. AIAA 2014-2498, 2014.

[24]Fedorov, A., Bres, G., Inkman, M., and Colonius, T., "Instability of hypersonic boundary layer on a wall with resonating micro-cavities," *49th AIAA Aerospace Sciences Meeting*, , No. AIAA 2011-373, 2011.

[25]Bres, G., Inkman, M., Colonius, T., and Fedorov, A., "Second-mode attenuation and cancellation by porous coatings in a high-speed boundary layer," *Journal of Fluid Mechanics*, Vol. 726, 2013, pp. 312–337.

[26]Wagnild, R., *High Enthalpy Effects on Two Boundary Layer Disturbances in Supersonic and Hypersonic Flow*, Ph.D. thesis, University of Minnesota, 240 Williamson Hall, 231 Pillsbury Drive S.E., Minneapolis, MN 55455, May 2012.

[27]Salemi, L., Fasel, H., Wernz, S., and Marquart, E., "Numerical Investigation of Wave-packets in a Hypersonic High-Enthalpy Boundary-Layer on a 5 Degree Sharp Cone," *7th AIAA Theoretical Fluid Mechanics Conference*, , No. AIAA 2014-2775, 2014.

[28]Salemi, L., Fasel, H., Wernz, S., and Marquart, E., "Numerical Investigation of Nonlinear Wave Packets in a Hypersonic High-Enthalpy Boundary Layer on a 5 Degree Sharp Cone," *45th AIAA Thermophysics Conference*, , No. AIAA 2015-2318, 2015.

[29]Salemi, L. and Fasel, H., "Linearized Navier-Stokes Simulations of the Spatial Stability of a Hypersonic Boundary-Layer on a Flared Cone," *53rd AIAA Aerospace Sciences Meeting*, , No. AIAA 2015-0838, 2015.

[30]Salemi, L., Gross, A., Fasel, H., Wernz, S., and Marquart, E., "Linearized Navier-Stokes Calculations of the Spatial Stability of a Hypersonic Boundary Layer on a 5 °Sharp Cone with High Temperature Effects," *52nd Aerospace Sciences Meeting*, , No. AIAA 2014-0430, 2014.

[31]Tumin, A., Private Communication, 2016.

[32]Edwards, L. and Tumin, A., "Real Gas Effects on Receptivity to Kinetic Fluctuations: I. Mean Flow Effect," *AIAA 2017-0070*, 2017.

[33]Fedorov, A. and Tumin, A., "Receptivity of High-Speed Boundary Layers to Kinetic Fluctuations," *AIAA 2016-3191*, 2016.

[34]Mortensen, C. H. and Zhong, X., "High-Order Shock-Fitting Method for Hypersonic Flow with Graphite Ablation and Boundary Layer Stability," *AIAA 2012-3150*, 2012.

[35]Mortensen, C. H. and Zhong, X., "Numerical Simulation of Graphite Ablation Induced Outgassing Effects on Hypersonic Boundary Layer Receptivity over a Cone Frustum," *AIAA 2013-0522*, 2013.

[36]Mortensen, C. H. and Zhong, X., "Real Gas and Surface Ablation Effects on Hypersonic Boundary Layer Instability over a Blunt Cone," *AIAA 2013-2981*, 2013.

[37]Mortensen, C. H. and Zhong, X., "Simulation of Second-Mode Instability in a Real-Gas Hypersonic Flow with Graphite Ablation," *AIAA Journal*, Vol. 52, No. 8, 2014, pp. 1632–1652.

[38]Mortensen, C. H. and Zhong, X., "Numerical Simulation of Hypersonic Boundary-Layer Instability in a Real Gas with Two-Dimensional Surface Roughness," *AIAA 2015-3077*, 2015.

[39]Mortensen, C. H., *Effects of Thermochemical Nonequilibrium on Hypersonic Boundary-Layer Instability in the Presence of Surface Ablation and Isolated Two-Dimensional Roughness*, Ph.D. thesis, University of California Los Angeles, 2015.

[40]Park, C., *Nonequilibrium Hypersonic Aerothermodynamics*, John Wiley & Sons Inc., New York, 1990.

[41]Lee, J., "Basic Governing Equations for the Flight Regimes of Aeroassisted Orbital Transfer Vehicles," *Thermal Design of Aeroassisted Orbital Transfer Vehicles*, edited by H. F. Nelson, Vol. 96, AIAA, 1985, pp. 3–53.

[42]Blottner, F., Johnson, M., and Ellis, M., "Chemically Reacting Gas Viscous Flow Program for Multi-Component Gas Mixtures," Tech. Rep. SC-RR–70-754, Sandia National Laboratories, 1971.

[43]Wilke, C., "A Viscosity Equation for Gas Mixtures," *The Journal of Chemical Physics*, Vol. 18, No. 4, 1950, pp. 517–519.

[44]Zhong, X., "High-Order Finite-Difference Schemes for Numerical Simulation of Hypersonic Boundary-Layer Transition," *Journal of Computational Physics*, Vol. 144, No. 2, 1998, pp. 662–709.

[45]Liu, Y. and Vinokur, M., "Nonequilibrium Flow Computations. I. An Analysis of Numerical Formulations of Conservation Laws," *Journal of Computational Physics*, Vol. 83, No. 2, 1989, pp. 373–397.

[46]Prakash, A., Parsons, N., Wang, X., and Zhong, X., "High-order Shock-fitting Methods for Direct Numerical Simulation of Hypersonic Flow with Chemical and Thermal Nonequilibrium," *Journal of Computational Physics*, Vol. 230, No. 23, 2011, pp. 8474–8507.

[47]Williamson, J., "Low-Storage Runge-Kutta Schemes," *Journal of Computational Physics*, Vol. 35, No. 1, 1980, pp. 48–56.

[48]Malik, M. and Spall, R., "On the stability of compressible flow past axisymmetric bodies," *Journal of Fluid Mechanics*, Vol. 228, 1991, pp. 443–463.

[49]Hudson, M. L., *Linear Stability of Hypersonic Flows in Thermal and Chemical Nonequilibrium*, Ph.D. thesis, North Carolina State University, 1996.

[50]Klentzman, J., Ulker, E., and Tumin, A., "Projection of the solution of the linearized Navier-Stokes equations in reacting high speed boundary layers onto discrete modes," *AIAA 2012-3149*, 2012.

[51]Anderson, E., Bai, Z., Bischof, C., Blackford, S., Demmel, J., garra, J. D., Croz, J. D., Greenbaum, A., Hammarling, S., McKenney, A., and Sorensen., D., *LAPACK Users' Guide*, Society for Industrial and Applied Mathematics, Philadelphia, PA, 3rd ed., 1999.

[52]Ma, Y. and Zhong, X., "Receptivity of a supersonic boundary layer over a flat plate. Part 1. Wave structures and interactions," *Journal of Fluid Mechanics*, Vol. 488, 2003, pp. 31–78.

[53]Gaydos, P. and Tumin, A., "Multimode Decomposition in Compressible Boundary Layers," *AIAA Journal*, Vol. 42, No. 6, 2004, pp. 1115–1121.

[54]Miselis, M., Huang, Y., and Zhong, X., "Modal Analysis of Receptivity Mechanisms for a Freestream Hot-Spot Perturbation on a Blunt Compression-Cone Boundary Layer," *AIAA 2016-3345*, 2016.

[55]Fedorov, A. and Khokhlov, A., "Excitation of Unstable Modes in a Supersonic Boundary Layer by Acoustic Waves," *Fluid Dynamics (Izvestiya Akademii Nauk SSSR, Mekhanika Zhidkosti i Gaza)*, Vol. 26, No. 4, 1991, pp. 531–537.

[56]Fedorov, A. and Khokhlov, A., "Prehistory of Instability in a Hypersonic Boundary Layer," *Theoretical Computational Fluid Dynamics*, Vol. 14, No. 6, 2001, pp. 359–375.

[57]Fedorov, A., "Receptivity of a High-Speed Boundary Layer to Acoustic Disturbances," *Journal of Fluid Mechanics*, Vol. 491, 2003, pp. 101–129.

[58]Gushchin, V. and Fedorov, A., "Excitation and Development of Unstable Disturbances in a Supersonic Boundary Layer," *Fluid Dynamics (Izvestiya Akademii Nauk SSSR, Mekhanika Zhidkosti i Gaza)*, Vol. 25, No. 3, 1990, pp. 344–352.

[59]Fedorov, A. and Tumin, A., "High-speed boundary-layer instability: old terminology and a new framework," *AIAA Journal*, Vol. 49, No. 8, 2011, pp. 1647–1657.